Sediment Transport Modeling Based on Geological Data for Holocene Coastal Evolution: Wave Source Estimation of Sandy Layers on the Coast of Hidaka, Hokkaido, Japan

Ryo Nakanishi[1,2,*] and Juichiro Ashi[1,2]

[1]Atmosphere and Ocean Research Institute, The University of Tokyo, Kashiwa, 277-8564, Japan.

[2] Graduate School of Frontier Sciences, The University of Tokyo, Kashiwa, 277-8561, Japan.

Corresponding author: Ryo Nakanishi (n-ryo@g.ecc.u-tokyo.ac.jp)

Key Points:

- Sediment transport is modeled in prehistoric periods by obtaining parameters as paleogeography and roughness from geological data
- A tsunami induced by a Kuril Trench earthquake reproduced the distribution and sedimentary structure of prehistoric sand layers
- Sensitivity tests revealed parameters that have a significant effect on sediment transport modelings in prehistoric periods

Abstract

Sediment transport modeling (STM) is a potentially effective tool for estimating the magnitude of tsunamis and earthquakes without historical records. However, applying STM to prehistorical tsunamis is challenging because of many uncertainties in topography and roughness. In the coast of Hidaka, Hokkaido, Japan, there is potential to conduct STM even in the absence of historical records because of the comprehensive geological data that reveal the coastal evolution during the Holocene in addition to tsunami sediment surveys. The tsunami deposits in Hokkaido suggest the presence of events on a larger scale than historical tsunamis; particularly the 17th-century tsunami had multiple potential wave sources other than a Kuril Trench earthquake, inhibiting its magnitude estimation. In this study, we applied STM to paleotsunamis in the coast of Hidaka, where the wave source is unknown and there are comprehensive geological data. The modeling parameters—paleotopography, roughness, grain size, initial sand source, sea level, and beach ridge height—were estimated using data obtained from geological surveys and sensitivity tests. The modeling of a tsunami induced by a Kuril Trench earthquake reproduced the sediment distributions and sedimentary structures of the observed sand layers better than that of the extreme storm and volcanic tsunami. The paring down wave sources of the sand layer implies

that a wider rupture zone in the Kuril Trench is less likely. This case study provides information on the parameters that geologists and modelers should consider when applying STM to paleotsunamis.

Plain Language Summary

Sediment transport modeling (STM) can correctly reproduce extreme waves caused by tsunamis and storms based on sedimentary evidence. However, applying it to prehistorical periods is challenging because of uncertainties in paleotopography. In the coast of Hidaka, Hokkaido, Japan is suitable area for STM because of the comprehensive geological data that reveal the coastal evolution during the Holocene in addition to tsunami sediment surveys. In this study, we established realistic computational parameters for STM based on detailed geological data and estimated wave sources for the sand layers formed by extreme waves. By comparing the observed sediment distribution or sedimentary structures and those estimated from the transport processes by the modeling of tsunami and extreme storm models, most of the sand layers were found to be tsunami deposits. This result allowed us to estimate the extent of the largest class of rupture zones in the Kuril Trench. Additionally, sensitivity tests for computational parameters with large uncertainties in the prehistoric period provide geologists and modelers important information that should consider when applying STM to paleotsunamis.

1 Introduction

Tsunami deposits are the few physical evidence that can be used to estimate the magnitude of earthquakes in the prehistorical period. Since the historic records in Hokkaido is limited to ~200 years, it is essential to reconstruct paleoearthquakes using tsunami deposits. To estimate the rupture zone of paleoearthquakes from tsunami deposits, conducting surveys at multiple sites and assuming a tsunami that comprehensively reconstructs correlated tsunami deposits at each site are necessary. Other factors, such as storms and floods should also be comprehensively examined to confirm that the event layers are tsunami deposits. Modern tsunami deposit studies have reported cases where the sand distribution does not correspond to the inundation area (Abe et al., 2012). The numerical simulation of sediment transport via extreme waves is a solution to the problems (Watanabe et al., 2018, 2021; Sugawara et al., 2019). Because directly comparing the distribution of sand layers with simulated tsunami inundation is impossible, tsunami propagation and associated sediment transport modeling (STM) have attracted considerable research attention (Sugawara et al., 2014a). Sugawara et al. (2019) estimated a rupture zone based on STM for a historical earthquake with an unknown fault model in Taiwan. They also suggested applying the estimation to historic tsunamis with no documented records. However, STM includes many parameters other than tsunami inundation simulation that can affect the results, and much uncertainty exists in simulated paleotsunami sediment transport (Apotsos et al. 2011a; Sugawara, 2019). If STM can be adapted to prehistoric periods, it can provide not only a proxy for interpreting of the formation origins of event layers but also the magnitude of paleotsunami to restrict source fault parameters.

The coastal areas of Hokkaido are suitable for a STM practice since geological data on the depositional environment has been reported in addition the little influence of artificial alteration and the wide distribution of wetlands. Since historical records in Hokkaido are limited to ~200 years, it is important to reconstruct paleoearthquakes using tsunami deposits. Geological

surveys along the Pacific coast of Hokkaido facing the Kuril Trench have suggested the occurrence of Mw (moment magnitude) >8 earthquakes in the southern Kuril Trench (Nanayama et al., 2003; Sawai et al., 2009; Sawai, 2020). Generally, tsunami deposits associated with the 17th century earthquake are distributed farther inland than other observed tsunami traces, and Mw 8.8 has been estimated using tsunami simulations (Ioki & Tanioka, 2016; Nakanishi et al., 2021). In these simulations, the source fault parameters are chosen to reproduce an inundation area covering the distribution of tsunami deposits at some survey sites along the Pacific coast of eastern Hokkaido (Figure 1b). Moreover, the tsunami deposits in the 17th century have been reported in the western Hokkaido from the Hidaka to Iburi regions. To reproduce tsunami deposits from western to the eastern Hokkaido by the same earthquake, a more extensive rupture zone than the conventional model (Sawai, 2020). Moreover, the 17th-century tsunami generation events do not only include the earthquake in the Kuril Trench but also the AD 1640 Mt. Komagatake collapse and the 1611 Keicho tsunami (Figure 1), which potentially originated in the Japan Trench, and their wave height distribution in Hokkaido are unknown. The multiple tsunami candidates complicate the magnitude estimation of Kuril earthquakes. To determine the extent of the rupture zone, comprehensive data must be obtained, especially filling in the blanks between the western and eastern Hokkaido. Therefore, Nakanishi et al. (2022) conducted a geological survey to investigate the western extent of tsunami deposits derived from Kuril earthquakes in the Shizunai area in the central Hidaka coast (Figure 1b). Consequently, seven tsunami deposit candidate layers were found, and one of them was suggested as a 17th-century event. However, whether sand layers were caused by either tsunamis or storms based on sedimentological features alone, was difficult to determine because the sand distribution were limited in the coastal area. Further, because the tsunami deposit candidate layers are located between Mt. Komagatake and the Kuril Trench (Figure 1), numerical simulations are essential to estimate their wave sources.

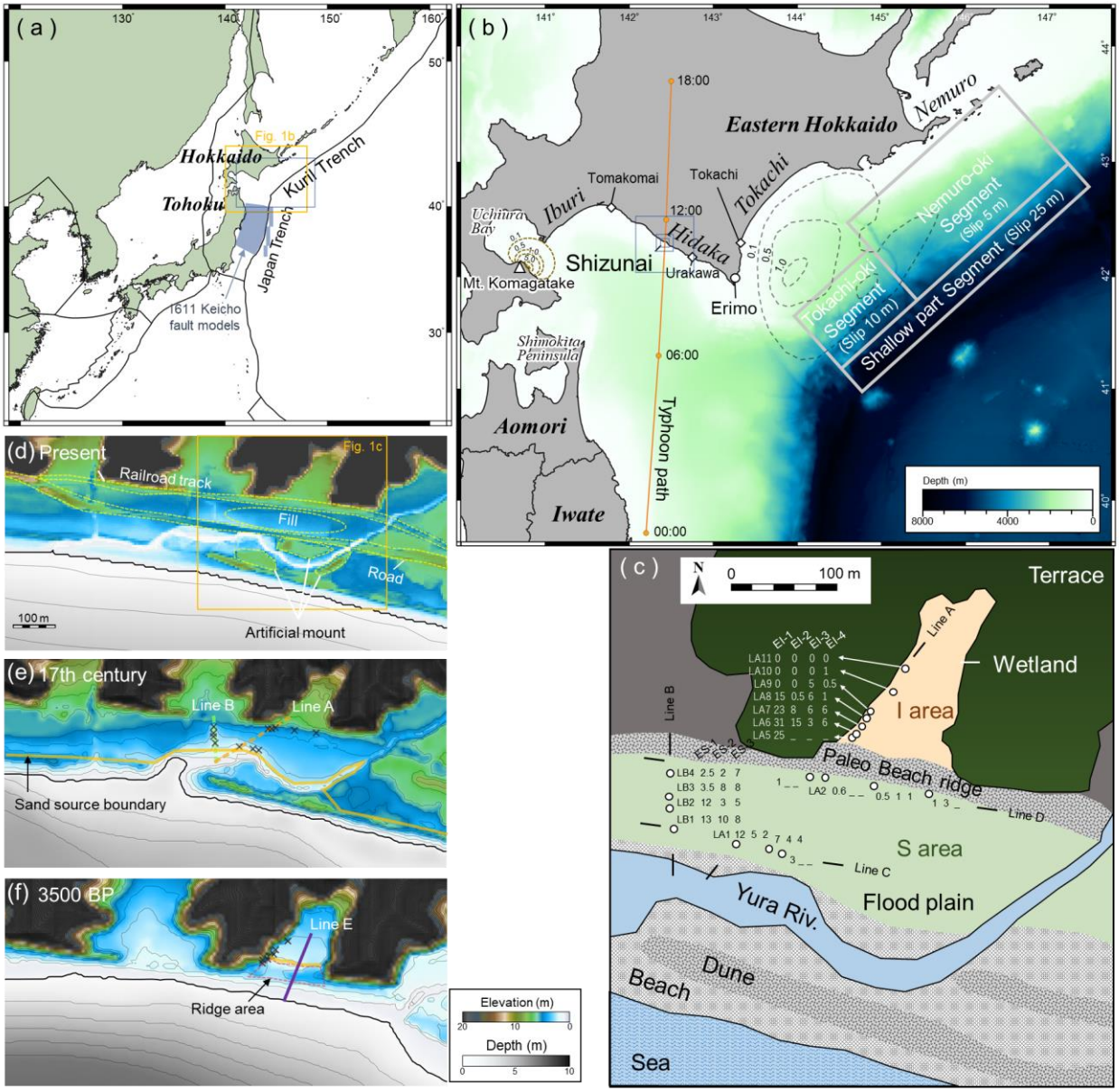

Figure 1. Maps of the study area. (a) Overall view of Japan and the plate boundary; the blue line indicates the computational domain (405 m mesh), and the blue-fill zones indicate the wave-source area of the 1611 Keicho tsunami in Imai et al. (2015)'s model. (b) Bathymetry of Northern Japan, showing the rupture zone of the 17th-century Kuril Trench earthquake model (gray boxes: Nakanishi et al., 2021), the initial water level due to the collapse of Mt. Komagatake in 1640 (brown broken lines: Nakanishi & Okamura, 2019), and the path of the typhoon model used in the numerical simulation; the gray broken lines show the initial water level of the 2003 Tokachi-oki earthquake tsunami used to validate the tsunami simulations (Romano et al., 2010), and the blue boxes indicate the computational domains (135-, 45-, 15-m meshes). (c) Geological overview map showing the boring sites. The thickness of each sand layer is marked beside the boring sites. (d) DEM data of the Shizunai area; the dotted lines delineate the zone of artificial land improvement, and contour lines are 1 m apart. (e) Paleogeography reconstructed from geological data of the Shizunai area around the 17th century; the solid yellow line indicates the boundary of the initial sand-source area, the black crosses indicate the distribution of ES-1, and the dashed lines indicate the survey lines. (f) Paleotopography (high ridge scenario) around 3500 BP; the red dashed line indicates the PBR zone, which is the assumed variable, the solid yellow line indicates the boundary of the source sand, the black crosses indicate the distribution of EI-4, and the purple line indicates the survey Line E.

In this study, we probed prehistoric tsunami- and storm-induced STM for event layers with an unknown wave source in the Shizunai area, paring down some possible wave sources. To apply STM in a prehistoric period, we attempted to reconstruct paleogeography based on geological information. The parameters difficult to identify were obtained from sensitivity tests, and the effect on STM was discussed. Not only the thicknesses of sand layers, which are usually used for validation, but also sedimentary structures based on the timeseries variation in sediment transport were examined. This study provides essential information on the computational parameters that modelers should consider and the geological information that geologists should collect when applying STM to paleotsunamis. By comparing the simulated and observed sediment features, we estimated which tsunami caused the event layers and finally discuss the rupture zone of the Kuril Trench.

2 Study Area

The southern part of the Kuril Trench is being subducted at a rate of ~8 cm/yr (Sella et al., 2002), and M 7–8 earthquakes occur at intervals of 50–100 years (Satake, 2015). These earthquakes occur within in the Tokachi-oki and Nemuro-oki segments, with fault lengths of 100–150 km. The most recent earthquake in the Tokachi-oki segment occurred in 2003, and a fault model of Mw 8.1 was estimated on the basis of a joint inversion of geodetic and tsunami data (Romano et al., 2010). The runup height of the tsunami generated by this earthquake was less than 2 m along the Hidaka coast (Tanioka et al., 2004).

Our study area is the Shizunai area located in the central coast of Hidaka, Hokkaido, where Nakanishi et al. (2022) conducted a detailed geological survey (Figure 1c). The alluvium in the Hidaka area comprises wave-dominated sandy beach deposits that form a Holocene beach ridge system. A paleobeach ridge (PBR), formed after the mid-Holocene highstand, was observed 300 m from the current coastline (Figure 1c). Peat wetlands are developed behind the PBR (I area), and floodplain sediments are distributed on the seaward side (S area). Because there is no tide station in the surrounding area, the mean higher high water and highest astronomical tide for the past 3 years at Tomakomai and Urakawa, neighboring tide stations, were used as a reference (Figure 1b). The mean higher high water and highest astronomical tide are, respectively, 0.37 and 0.60 m at Urakawa and 0.44 and 0.65 m at Tomakomai. Thus, for the study area assumed 0.4 and 0.6 m, respectively.

2.1 Observed Sand Layers

ES-1 (ca. 17th century), ES-2, and ES-3 (ca. 7th–10th century) have been identified as anomalous sand layers in the S area (Nakanishi et al., 2022). ES-1 is distributed over the entire S area but does not exceed the PBR, and ES-2 and ES-3 are distributed almost similarly to ES-1 (Figure 1c). From the river's mouth to the northeast, the sand layers are thinning. Vertical grain-size changes of the sand layers show a single normal grading structure. In the I area, four event layers (from top to bottom, EI-1, EI-2, EI-3, and EI-4) have been reported between 4,000 and 3,000 BP, and the sand layers tend to thin inland (Figure 1c). EI-3 and EI-4 are distributed sheet-like, whereas the thicknesses of EI-1 and EI-2 change from a few tens of centimeters to an unrecognizable layer at a distance of ~50 m from the PBR. In EI-1, the grain-size composition is poorly sorted, with a repeated grading structure, whereas the other sand layers show either an inverse-normal grading or a single normal grading structure. Nakanishi et al. (2022) concluded

that the event layers, except for EI-1, are probably tsunami deposits because they have similar features to the deposits reported in observed tsunamis. ES-1, EI-3, and EI-4 are in the range of tsunami recurrence age in the eastern Hokkaido coast, suggesting that they have been derived from tsunamis originating from earthquakes in the Kuril Trench. However, because the distribution of the sand layers is around 100 m from the coastline, there is still a possibility that the sand layers were deposited by extreme storms. Furthermore, there are multiple tsunami wave source candidates for the 17th century event, but these have not been discussed in detail.

2.2 Relative Sea Level Changes

To reconstruct the paleomorphology for STM, it was necessary to estimate the relative sea level (RSL) at the time of the events. The RSL changes in Shimokita Peninsula (Figure 1b), based on geological evidence and associated with ice sheet melting during the Holocene, indicate a mid-Holocene highstand range of 0.7–2.1 m, with a peak at 4,000–3,000 BP (Yokoyama et al., 2012). In the Shizunai area, the mid-Holocene highstand, estimated from a glacial isostatic adjustment (GIA) model without considering crustal movement, is 0.5–2.5 m (Okuno et al., 2014). The marine terrace heights of marine isotope stages (MISs) 5e and 7 around Shizunai range in 45–55 and 85–90 m, respectively (Koike & Machida, 2001). Considering the 4–13.5 m sea-level rise in MIS 5e due to GIA (Okuno et al., 2014), the uplift rate was calculated to be 0.25–0.40 mm/yr, with a similar uplift rate over MIS 7. Nakanishi et al. (2022) reported sea-level index points corresponding to the mean higher high water and highest astronomical tide based on diatom assemblages and chemical analyses. Comparing these results with the RSL changes based on the GIA model (Figure 2), the trends of the changes were consistent, but the sea-level index points were 1–2 m higher between 5,000 and 4,000 BP. The GIA model shows a difference of ~1 m between the Shimokita Peninsula and Shizunai area, which reflects regional isostatic differences (Okuno et al., 2014). Therefore, we varied the slope of the RSL curve to a tangent of the sea-level index points. The revised RSL curve based on sea-level index points at 4 m above present sea level (asl) during 5,000–4,000 BP agreed with the sea-level index points around 1,300 BP, which was also within the range of the 6,000-BP RSL estimated by Okuno et al. (2014). The sea-level index points at 5 m asl were rejected because the estimated mean sea level exceeded the sea-level index points around 1,300 BP and the RSL based on the GIA model. According to this estimation curve, the estimated RSL at the time of the events was ~0.3-m asl during the 17th century (ES-1), ~1 m asl during the 7th–10th centuries (ES-2 and ES-3), 3–3.5 m asl from 3,500 to 3,000 BP (EI-1 and EI-2), and 3.5–4 m asl from 4,000 to 3,500 BP (EI-3 and EI-4). As the paleo-sea level and tide level at the time of the event could not be uniquely determined, we estimated the paleo-sea level from the RSL change curves for each event occurrence considering the current tidal change levels ($\pm$0.5 m) as the error.

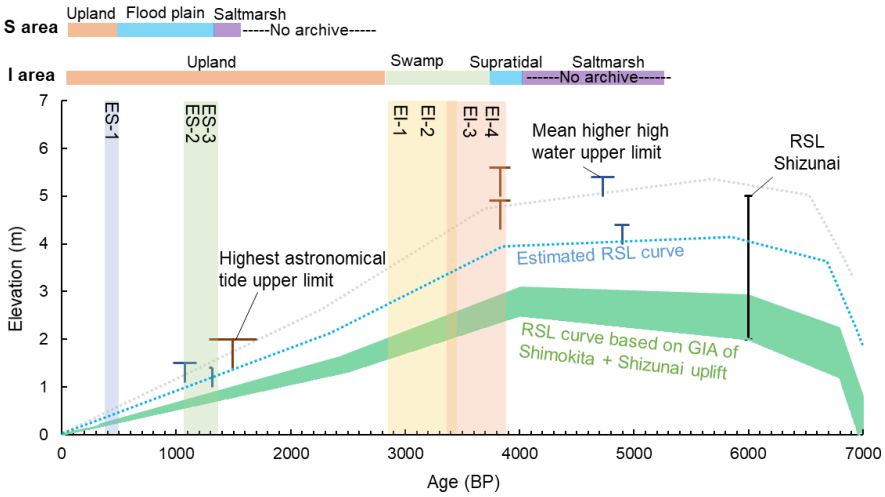

Figure 2. Estimated RSL change curves in the Shizunai area. The green-fill displays a RSL curve estimated from the GIA model around the Shimokita Peninsula (Yokoyama et al., 2012) and the crustal deformation range of the Shizunai area. Black bars indicate the RSL estimated by Okuno et al. (2014)'s GIA model with crustal deformation around the Shizunai area. The T-shape indicates the sea-level index points with error as the tide ranges in the Shizunai area (Nakanishi et al., 2022). The blue dotted and gray lines show the estimated RSL curve adjusted to the sea-level index points and the rejected RSL curve, respectively. The color bars indicate the paleodepositional environment and depositional age of the sand layers in the Shizunai area (Nakanishi et al., 2022).

2.3 Paleogeomorphology

To reproduce the paleogeomorphology, 5-m mesh data were used to eliminate artificial structures (i.e., roads and railroad tracks) and reconstruct the estuary, beach ridge, and ground surface based on the geological information (Figure 1d–f). The paleotopographies of the 17th century and 3,500 BP were created. Artificial structures and embankments were removed as the 17th-century topography (Figure 1d) based on aerial photographs from the 1940s and topographic maps from the 1880s. Landowner interviews determined that the pastureland in the S area had been reclaimed. The elevation of the 17th-century ground surface was interpolated using the depth of AD 1663 Usu tephra obtained from the pasture periphery. According to Nakanishi et al. (2022), brackish water entered around the river mouth (Line C: Figure 1c). Therefore, the steep landform that separates the S area from the river mouth (now covered by a national highway) was smoothed. Based on the 1940s' aerial photographs, we assumed that the Yura River flowed directly to the sea. The presence of old rivers along Line B and the low organic matter content of the river floodplain before the 17th century suggested that the S area was a lowland with little vegetation. The shallow bathymetry was supplemented from the surrounding area data because no data were available. Detailed shallow-water isobath in Tomakomai (Japan Coast Guard, 1982), located northwest of Shizunai (Figure 1b), shows generally smooth topography along the coastline, with slopes ranging from 7/1000 to 5/1000. The shallow bathymetry of the study area was interpolated to follow a ~6/1000 slope. The 17th century bathymetry reconstructs a gently sloping fan-delta topography in front of the river mouth.

The 3,500-BP topography was created as the period from the mid-Holocene highstand to the sea regression when the PBR was a beach (Figure 1f). The topography was revised to the basal level of the EI-4 layer. The PBR was assumed to have gradually developed from a tidal flat

environment before 5,000 BP and reached its current height around 2,000 BP, based on the distribution of volcanic ash (Nakanishi et al., 2022). Seawater inflow ceased around 4,000 BP, which was considered the initial stage of PBR formation. It was assumed that the development of the PBR was progressing since the depositional environment was closed during 3,500–3,000 BP. However, we were unable to obtain any materials to estimate the exact height of the PBR when the event occurred. Dune and embankment heights considerably affect an inundation and sand-layer distribution (Sugawara, 2019). Therefore, we assumed the intermediate ridge (medium ridge) height between the current PBR height (high ridge) and flat topography (low ridge). The current PBR is slightly lower in the middle area parallel to the shore, as reflected in the shape of all beach ridges (Figure 1f). The seaward side of the PBR was reconstructed as a gently sloping beach. The coastline and isobath were designed parallel to the marine erosion cliffs and the distance from PBR depend on the estimated sea levels and slope. The seafloor slope is estimated to have changed, reflecting the dynamic equilibrium due to sea-level rising (Bruun, 1962). Therefore, the slope was estimated from the beach ridge migration and sea level rise using the Bruun rule (Bruun, 1962). The shallow-water bathymetry was interpolated with a slope of 9/1000–16/1000 based on the results.

3. Methods

3.1 Wave Propagation and Sediment Transport

Wave propagation calculation and STM were performed using Delft-3D (Delfters, 2020), which has been employed to reproduce many observed tsunamis and storm surges and laboratory experiments (see, e.g., Apotsos et al., 2011a, b, c; Lesser et al., 2004; Li & Huang, 2013; van Ormondt et al., 2020; Watanabe et al., 2017, 2018). The governing equations comprise horizontal depth-averaged momentum equations, a depth-averaged continuity equation, and a transport equation (Delfters, 2020). Particularly, the wave propagation calculation used Delft-3D Flow module nonlinear shallow water equations with a finite difference scheme on a staggered grid (Stelling & van Kester, 1994). The reproducibility of the tsunami simulation was verified using the 2003 Tokachi-oki earthquake fault model and tsunami data (Romano et al., 2010). The results of the Delft-3D simulation were comparable to those of Romano et al. (2010) for the coastal areas of Tokachi and Hidaka (Figure S1). Storm hydrodynamics was calculated by coupling the Delft-3D-Flow module and SWAN (Booij et al., 1999; Watanabe et al., 2017, 2018). Because storm surges are strongly influenced by tides, tidal change was obtained from the TPXO7.2 database as the base boundary condition. Storm waves due to wind were calculated by SWAN, and the Flow module was employed for the wave propagation calculations using alternately handing over data.

Topography and bathymetry data were nested at 405, 135, 45, 15, and 5-m mesh sizes. The bathymetry data were from the Japan Oceanographic Data Center and the Japan Hydrographic Association M7000 series, whereas the topography data were from the ASTER GDEM, Version 3, Shuttle Radar Topography Mission and Geographical Survey Institute 5-m mesh digital elevation model (DEM). To stabilize the calculations, the time step for the 5-m mesh domain was set to 0.1 s, and the computation time was 3, 18, and 12 h for tsunamis, tide changes, and storm surge and wave, respectively. The tsunami wave heights were confirmed insufficient to cause land flooding after 3 h.

The bedload and suspended load transport of non-cohesive sediments were calculated in the 5-m mesh domain following van Rijn (1993). The sediment transport was solved as a coupled equation using the mass conservation and continuity equations in a single vertical layer to reduce the computational time; the coupled equation could reproduce realistic tsunami and storm deposits (Watanabe et al., 2017, 2018). The settling velocity was calculated following van Rijn (1993)'s method based on sediment diameter and the relative density of the grain size. The reference height for sediment exchange with a bed was based on the bed roughness at each step (van Rijn, 1993), and the thickness of the sediment was updated at every time step to reflect the transported sediment.

3.2 Tsunamis and Storm Source Models

Source candidates for the 17th century tsunami in the Hidaka region included the Kuril Trench earthquake, AD 1640 Mt. Komagatake collapse, and AD 1611 Keicho tsunami (Sawai, 2020; Nakanishi et al., 2022: Figure 1). A fault model was proposed for the 17th century Kuril Trench earthquake to simulate an inundation area that roughly covered tsunami deposits from Nemuro to Erimo (Satake et al., 2008; Ioki & Tanioka, 2016; Nakanishi et al., 2021). This model does not fully address the issues of the unknown extent of the rupture zone from east to west and too high wave heights in the Tohoku region (Satake et al., 2008). The tsunami induced by the collapse of Mt. Komagatake was described to have killed at least 700 people in historical documents (Nishimura & Miyaji, 1995). The estimated initial wave heights of this event reproduced tsunami deposits extending from Uchiura Bay to the western Iburi coast, consistent with the volume of debris that flowed into the sea (Nakanishi & Okamura, 2019). According to historical documents, the AD 1611 Keicho tsunami caused tremendous damage in the Tohoku region but no major seismic motions. Therefore, theories include tsunami earthquakes (i.e., in the outer rises or the Kuril Trench) and submarine landslides, but the wave sources are nonconsensual (Sawai, 2020); Imai et al. (2015) estimated the rupture zone (Mw 8.4–8.7) in the Japan Trench by inverting multiple faults based on the record of tsunami run-ups. However, the wave heights of these models are 2–3 m even in the northern Shimokita Peninsula (Figure 1a); thus, the tsunami heights in the Shizunai area are estimated to be about the same as those of historical tsunamis. We used the 17th-century earthquake (Ts: Nakanishi et al., 2021) model as the Kuril Trench earthquake to validate the wave source of the event layers in the Shizunai area (Figure 1b). This model, based on Ioki & Tanioka (2016)'s model, divides the area into three regions with different slip values: the Tokachi-oki segment, 10 m; the Nemuro-oki segment, 5 m, and the shallow segment, 25 m. The shallow segment was based on the shallow slip that caused high wave heights in the Tohoku region in 2011 (Satake et al., 2013). Additionally, the Tokachi-oki segment had a 70-km modified fault width to cover tsunami deposits in the Erimo area (Nakanishi et al., 2021). Although many uncertainties remain in the model, this study has not reached a model modification because it cannot be constrained a fault parameter by a single site study. The initial wave height by the crustal deformation was calculated using the Okada (1985)'s method. The AD 1640 Mt. Komagatake collapse tsunami was modeled under an initial wave height condition (Tv model: Figure 1b), which reproduced the tsunami deposits around Uchiura Bay (Nakanishi & Okamura, 2019). Because no fault model had established Kuril earthquakes before the 17th century, we tentatively used the Ts model for the older events.

It was necessary to consider if the deposits were caused by extreme storms because the distribution of the event layers is more limited than that of paleotsunami deposits reported in eastern Hokkaido. Because Hokkaido is located far north of the equator, it is rare for strong

typhoons to make landfall in this area (Table S1). Over the past 70 years, 27 typhoons have made landfall in Hokkaido, 19 of which landed on the Hidaka coast. Because determining the parameters of the largest typhoons of the late- to mid-Holocene in Hokkaido is difficult, we assume that the typhoon models were excessive scale of Hokkaido, judging from the observational record. These models are the largest storm in recorded history in Hokkaido (Sh) at 80 kt and 965 hPa, based on the wind speeds and minimum pressures of Typhoon Mireille in 1991 and Typhoon Shirley in 1965 (Table S1). A Japan's largest storm model (Sj) had a minimum pressure in all of Japan and maximum wind speed of 870 hPa and 140 kt, respectively, based on Typhoon Tip in 1979—the largest typhoon ever recorded in Japan. The parametric wind field was based on Holland et al. (2010)'s wind profile relationships. The radius of the typhoon was set to 250 and 370 km for the Sh and Sj models, respectively. The typhoon path was set to the highest wave height in the Shizunai area based on the path of Typhoon Chanthu (Figure 1a), which caused significant damage in 2016. The forward speed of the typhoon is 20 km/h, which is the most frequently recorded speed for typhoons approaching Hokkaido (Nakajo et al., 2013).

3.3 Sensitivity Testing

As well as wave height, STM is affected by topographic and sediment conditions (Apotsos et al., 2011b; Gusman et al., 2012, 2018; Li et al., 2012, 2014; Sugawara, 2019; Sugawara et al., 2014b, 2019; Watanabe et al., 2017, 2021). Therefore, we performed sensitivity tests in the realistic parameter ranges that may have affected STM (Table 1).

Table 1. Parameters of the sediment transport modeling scenario.

Sensitive test

Case	Initial bed	Sea level	Source roughness	Land roughness	Grain size	Bathymetory Slope
AIBM25	All area	+ 0.5 m	0.025	0.025	0.13 mm, 0.44 mm	6/1000
AIBM20	All area	+ 0.5 m	0.020	0.020	0.13 mm, 0.44 mm	6/1000
GS13	Sand area	+ 0.5 m	0.025	0.025	0.13 mm	6/1000
GS44	Sand area	+ 0.5 m	0.025	0.025	0.44 mm	6/1000
S25L25	Sand area	+ 0.5 m	0.025	0.025	0.13 mm, 0.44 mm	6/1000
S25L20	Sand area	+ 0.5 m	0.025	0.020	0.13 mm, 0.44 mm	6/1000
S25L30	Sand area	+ 0.5 m	0.025	0.030	0.13 mm, 0.44 mm	6/1000
S20L25	Sand area	+ 0.5 m	0.020	0.025	0.13 mm, 0.44 mm	6/1000
S30L25	Sand area	+ 0.5 m	0.030	0.025	0.13 mm, 0.44 mm	6/1000
S20L20	Sand area	+ 0.5 m	0.020	0.020	0.13 mm, 0.44 mm	6/1000
BS3	Sand area	+ 0 m	0.020	0.020	0.13 mm, 0.44 mm	3/1000
BS6	Sand area	+ 0 m	0.020	0.020	0.13 mm, 0.44 mm	6/1000
BS12	Sand area	+ 0 m	0.020	0.020	0.13 mm, 0.44 mm	12/1000

S area (ES-1~ES-3)

Scenario	Wave source	Adjusted level	Source roughness
Ts0mM20	17th century Kurile earthquake	0 m	0.020
Ts0mM25	17th century Kurile earthquake	0 m	0.025
Ts0.5mM20	17th century Kurile earthquake	+ 0.5 m	0.020
Ts0.5mM25	17th century Kurile earthquake	+ 0.5 m	0.025
Ts1mM20	17th century Kurile earthquake	+ 1 m	0.020
Ts1mM25	17th century Kurile earthquake	+ 1 m	0.025
Tv1mM20	Komagatake IWL98m	+ 1 m	0.020
Sj1mM20	Japan largest typhoon	+ 1 m	0.020
Sj1mM25	Japan largest typhoon	+ 1 m	0.025
Sh1mM20	Hokkaido largest typhoon	+ 1 m	0.020
Sh1mM25	Hokkaido largest typhoon	+ 1 m	0.025

I area (EI-1~EI-4)

Scenario	Wave source	Adjusted level	Source/Land roughness	Beach ridge height
Ts3mRh	17th century Kurile earthquake	+ 3 m	0.025	High
Ts3mRm	17th century Kurile earthquake	+ 3 m	0.025	Medium
Ts3.5mRh	17th century Kurile earthquake	+ 3.5 m	0.025	High
Ts3.5mRm	17th century Kurile earthquake	+ 3.5 m	0.025	Medium
Ts3.5mRl	17th century Kurile earthquake	+ 3.5 m	0.025	Low
Ts4mRm	17th century Kurile earthquake	+ 4 m	0.025	Medium
Ts4mRl	17th century Kurile earthquake	+ 4 m	0.025	Low
Sj3mRh	Japan largest typhoon	+ 3 m	0.025	High
Sj3mRm	Japan largest typhoon	+ 3 m	0.025	Medium
Sj3.5mRh	Japan largest typhoon	+ 3.5 m	0.025	High
Sj3.5mRm	Japan largest typhoon	+ 3.5 m	0.025	Medium
Sj3.5mRl	Japan largest typhoon	+ 3.5 m	0.025	Low
Sj4mRm	Japan largest typhoon	+ 4 m	0.025	Medium
Sj4mRl	Japan largest typhoon	+ 4 m	0.025	Low
Sh3mRh	Hokkaido largest typhoon	+ 3 m	0.025	High
Sh3mRm	Hokkaido largest typhoon	+ 3 m	0.025	Medium
Sh3.5mRh	Hokkaido largest typhoon	+ 3.5 m	0.025	High
Sh3.5mRm	Hokkaido largest typhoon	+ 3.5 m	0.025	Medium
Sh3.5mRl	Hokkaido largest typhoon	+ 3.5 m	0.025	Low
Sh4mRm	Hokkaido largest typhoon	+ 4 m	0.025	Medium
Sh4mRl	Hokkaido largest typhoon	+ 4 m	0.025	Low

Gray color indicates the scenarios no overflow scenarios

To confirm the influence of the initial source-sand thickness, STM was also performed under the condition that the entire area could be a sand source as a control experiment (Table 1). The entire sand source scenario (AIBM20) for both survey lines overestimated the source-sand area and layer thickness due to unrealistic sand sources (Figure 3); erosion occurred at sites where the mud was distributed as surface sediment according to the geological survey (Nakanishi et al., 2022). The initial source-sand thickness of the observed sediments was set as the distribution of sandy beaches and rivers based on the geological information (Figure 1e), indicating that the initial source-sand thickness was 0 m in the area where peatland and floodplain sediments were distributed. The initial source-sand thickness was confirmed to be greater than the maximum erosion thickness to ensure that the supply of sand is sufficient.

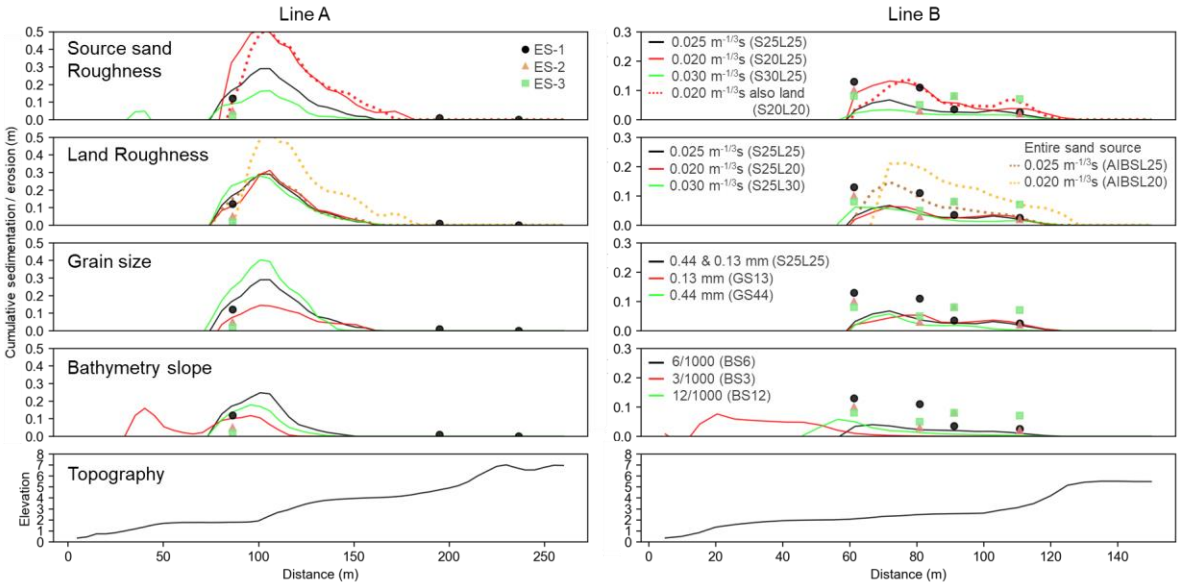

Figure 3. Sensitivity test results of STM along Lines A and B. Markers indicate the thickness of the observed sand layers. The scenario conditions are summarized in Table 1.

Because the roughness coefficient of sand sources significant effect on sediment transport (Li & Huang, 2013; Li et al., 2014; Sugawara et al., 2014b; Watanabe et al., 2017), we performed a control experiment using the reported Manning's roughness coefficient, ranging from 0.020 to 0.030 $m^{-1/3}s$ (Apotsos et al., 2011b; Kaiser et al., 2011; Kotani et al., 1998). Manning's roughness coefficients of 0.025 and 0.030 $m^{-1/3}s$ had the same distribution area, although the layer thicknesses were 1.5–2 times different (Figure 3). The scenario of Manning's roughness coefficient of 0.020 $m^{-1/3}s$ produced thicker layer and a wider inland distribution area, indicating that the roughness coefficient of the source was sensitive to STM. Therefore, calculations were performed using both the widely used condition of 0.025 $m^{-1/3}s$ and the condition of 0.020 $m^{-1/3}s$. Terrestrial roughness coefficients vary with land surface morphology and vegetation density (Jaffe et al., 2012; Kaiser et al., 2011; Kotani et al., 1998; Sugawara et al., 2014b). Based on geological information, the terrestrial environment in the I area in 4,000–3,000 BP was estimated to be supratidal to freshwater marsh (Nakanishi et al., 2022). The S area was estimated to have been bare ground with an organic matter concentration of < 1%. These ground surfaces were considered to have a Manning's roughness coefficient range of 0.020–0.030 $m^{-1/3}s$ (Jaffe et al., 2012; Kotani et al., 1998; Sugawara et al., 2014b). By only varying the terrestrial roughness coefficient, the results of STM were between 0.02 and 0.03 $m^{-1/3}s$, which did not considerably affect on the layer thickness distribution (Figure 3). Therefore, the S area was set to 0.020 $m^{-1/3}s$ as bare ground, and the I area was set to 0.025 $m^{-1/3}s$ as a water body based on Kotani et al. (1998). Seafloor roughness was set to 0.025 $m^{-1/3}s$ (Kotani et al., 1998).

The simulated grain-size composition was based on the event layers and sources. Based on grain size, the event layer sources were determined to be beach and estuarine sands. The mean diameters ranged from 1.0 to 0.125 mm for most sand layers, with modes at 0.44 and 0.13 mm (Nakanishi et al., 2022). As a sensitivity test, we used either a single grain size (0.13 or 0.44 mm) or mixed sand (1:1 ratio of 0.13 and 0.44 mm) to assess how the distribution changed (i.e., a normal distribution with D10 = 0.75 × D50 and D90 = 1.5 × D50). The single 0.44 mm case had

a narrow distribution area and thick layers, whereas the single 0.13 mm case had a wide distribution and thin layers (Figure 3). The mixed sand scenario showed a broad thin layer and a thick layer near the sand source. Gusman et al. (2018) suggested that mixed sand reproduces actual sediment well, so mixed sand close to the actual source grain size was used to monitor sedimentary structures.

The slope of the seafloor affects STM because it is related to reducing flow velocity. This study reproduced realistic seafloor topography with reference to the shallow-water bathymetry in the surrounding area, and the sensitivity for the extent of the estimated sediments when the slope differs was investigated. Sensitivity tests were performed on realistic and extreme isobaths with slopes of 3/1000 and 12/1000 (Figure 3). The 12/1000 slope scenario showed similar results to the realistic scenario, despite the twice higher angle. Because the 3/1000 slope is a stretch of shallow water, sand deposition begins seaward and does not extend inland due to deceleration offshore.

4 Results

4.1 Wave Form

The maximum tidal range used to calculate the storm was 2 m, with a peak at 11 hr (Figure 4). The storm track was set as land near Shizunai at the time of the tidal peak. In response to low atmospheric pressure, the Sj and Sh models simulated maximum wave heights of 2.5 and 1.5 m, respectively. The corresponding net water level rises due to the typhoon were 1.5 and 0.5 m. The wind direction changed from south–southeast to northwest after landfall.

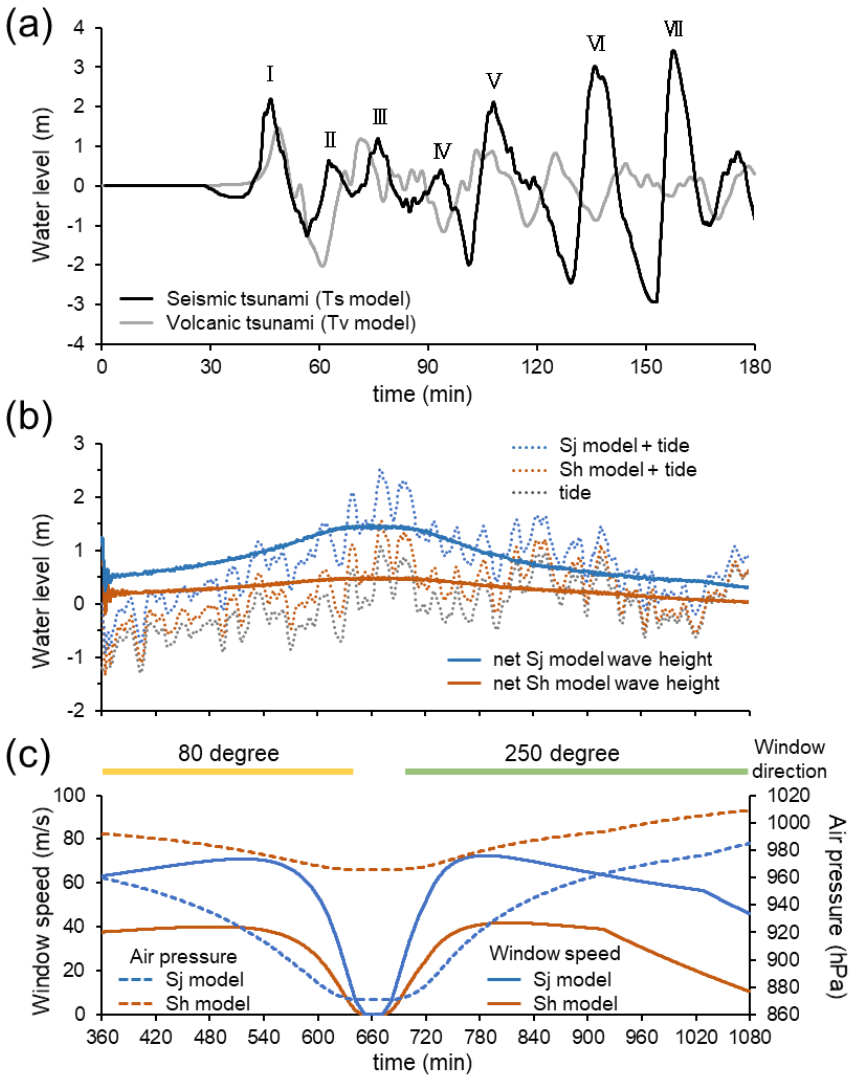

Figure 4. Wave amplitudes, atmospheric pressure and wind speed obtained by numerical simulations of the tsunami and storm models. (a) Amplitudes of tsunamis due to the 17th-century Kuril earthquake and 1640 mountain collapse. (b) Wave amplitudes induced by storms, accounting for tidal changes. (c) Timeseries of changes in air pressure and wind speed/direction caused by the storm models.

The tsunami induced by the Ts model was 0.5–2 m in the first to fourth waves off Shizunai, but the fifth to seventh waves tended to be higher, ranging from 2 to 3.5 m in height. These large amplitudes of subsequent waves were attributed to the edge waves and the tsunami caused by the 2003 Tokachi-oki earthquake (Tanioka et al., 2004; Supporting information S2). The tsunami induced by the Tv model had a maximum wave height of < 2 m in the first wave and a decaying profile after the second wave.

4.2 Modeling of 7th–17th Century Inundation and Sediment Transport

4.2.1 Tsunami models

The inundation path by the Ts model was limited to the river mouth due to the presence of 6-m-high dunes (Figure 5). The tsunami inundation area for all sea level scenarios did not exceed the PBR. Higher sea level scenarios tended to have wider inundation areas. The tsunami inflow eroded the entire river mouth, and sand was deposited immediately landward in both tsunami models (Figure 5a–g). The sediment thickness by the Ts model was thick near the estuary and thinner inland; this trend was the same regardless of the roughness coefficient and sea level. Higher sea level scenarios show wider sediment distributions, but the layer thickness does not change much (Figure 5a–c). Smaller scenarios for source roughness displayed slightly wider and thicker sand layers. The sediment transport by the Tv model only occurred within a limited area in the estuary, and there was little difference between the inundation area and sediment distribution (Figure 5g).

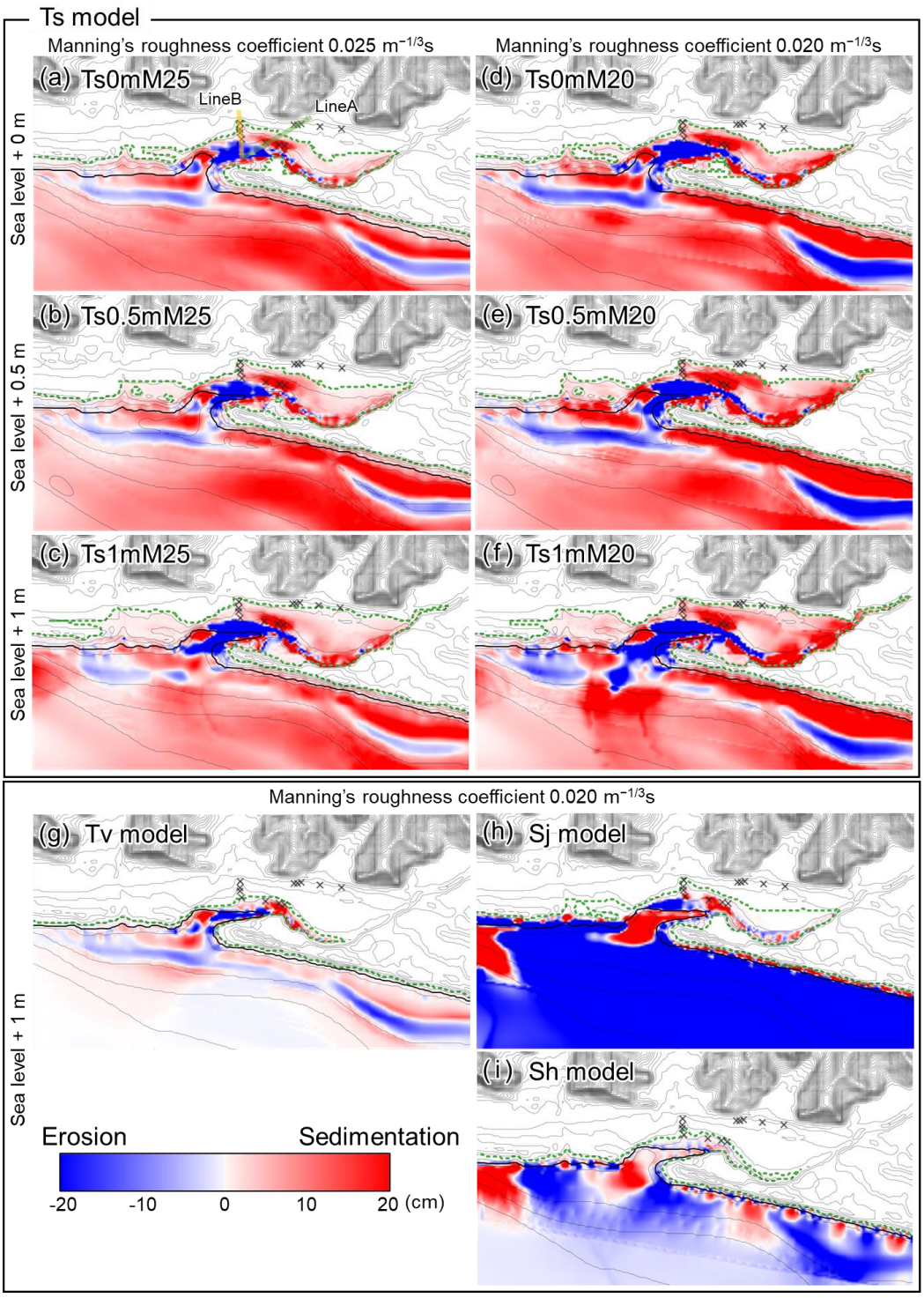

Figure 5. Cumulative sedimentation and erosion amount estimated using STM in the S area; the green dotted lines indicate the maximum inundation area; and the black crosses indicate the distribution of ES-1.

Figure 6 shows the succession of hydraulic conditions and sediment transport for the + 1 m sea level and 0.020 $m^{-1/3}s$ roughness scenario at LB1 (Figure 1c). An 8-cm sand layer was deposited by the first and sixth waves (Figure 6a). On the inflow of the seventh wave, the largest

wave, most sediment was eroded, and then a 5-cm sand layer was deposited. The return flow eroded ~1 cm sand, leaving a 4-cm sand layer. The grain size of the sand layer was 0.13 mm with twice the flux of the 0.44 mm component. These sands were transported only in suspension.

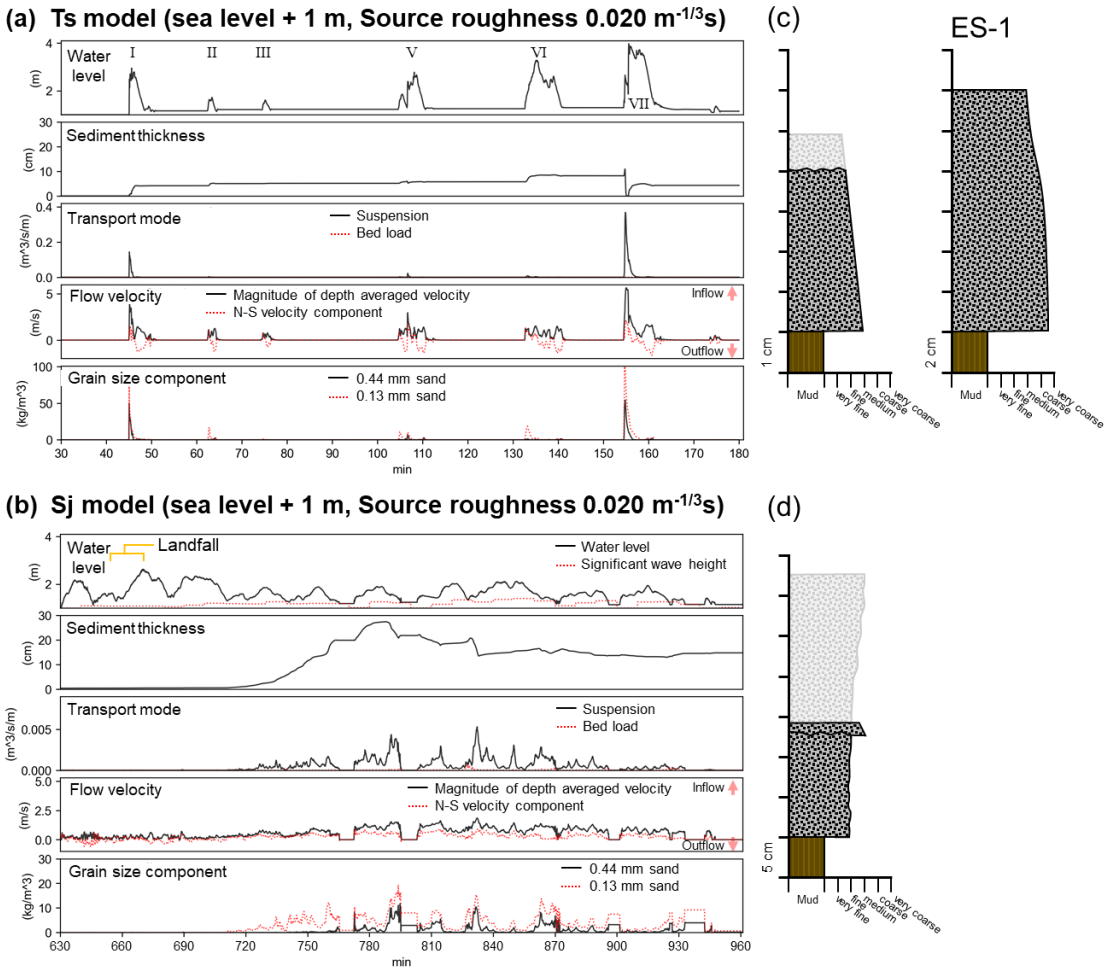

Figure 6. Timeseries of hydrodynamic and sediment transport and the sedimentary structures estimated using STMs at LB1. In the Ts (a) and Sj (b) models, the timeseries of water level, sediment thickness, transport flux for each transport mode, flow velocity, and transport flux for each grain-size composition are shown. The sedimentary structures inferred from STM using the Ts (c) and Sj (d) models, and observed ES-1.

4.2.2 Storm models

The inundation by the Sh and Sj models did not reach the PBR, even when the mean sea level was set to + 1 m (Figure 5hi). The erosion and sedimentation by the Sj model was limited to an area between the river mouth and land, showing discontinuous thickness distributions parallel to the coastline (Figure 5h). The Sh model showed little sediment transport (Figure 5i).

For the succession of hydraulic conditions, the Sj model at LB1 shows that the wave height increased after the typhoon landfall, and gradual sedimentation occurred in 720–790 min (Figure 6b). Therefore, ~10 cm of erosion occurred, but a return flow component was unobserved, so this sand was transported inland. The transport mode was suspension, although a temporary bed load was recognized. The sediments formed during landfall were mostly fine, but the coarse component increased when the layer thickness reached the maximum.

4.3. Simulation of 4,000–3,000 BP Inundation and Sediment Transport

The results are described for each sea-level scenario (Figure 7). Line E in the center of the I area perpendicular to the coastline was used as the survey line (Figure 1f) because the boring site was near a cliff and the mesh size of the DEM data was on average 5 m, which differed from the actual topography in places.

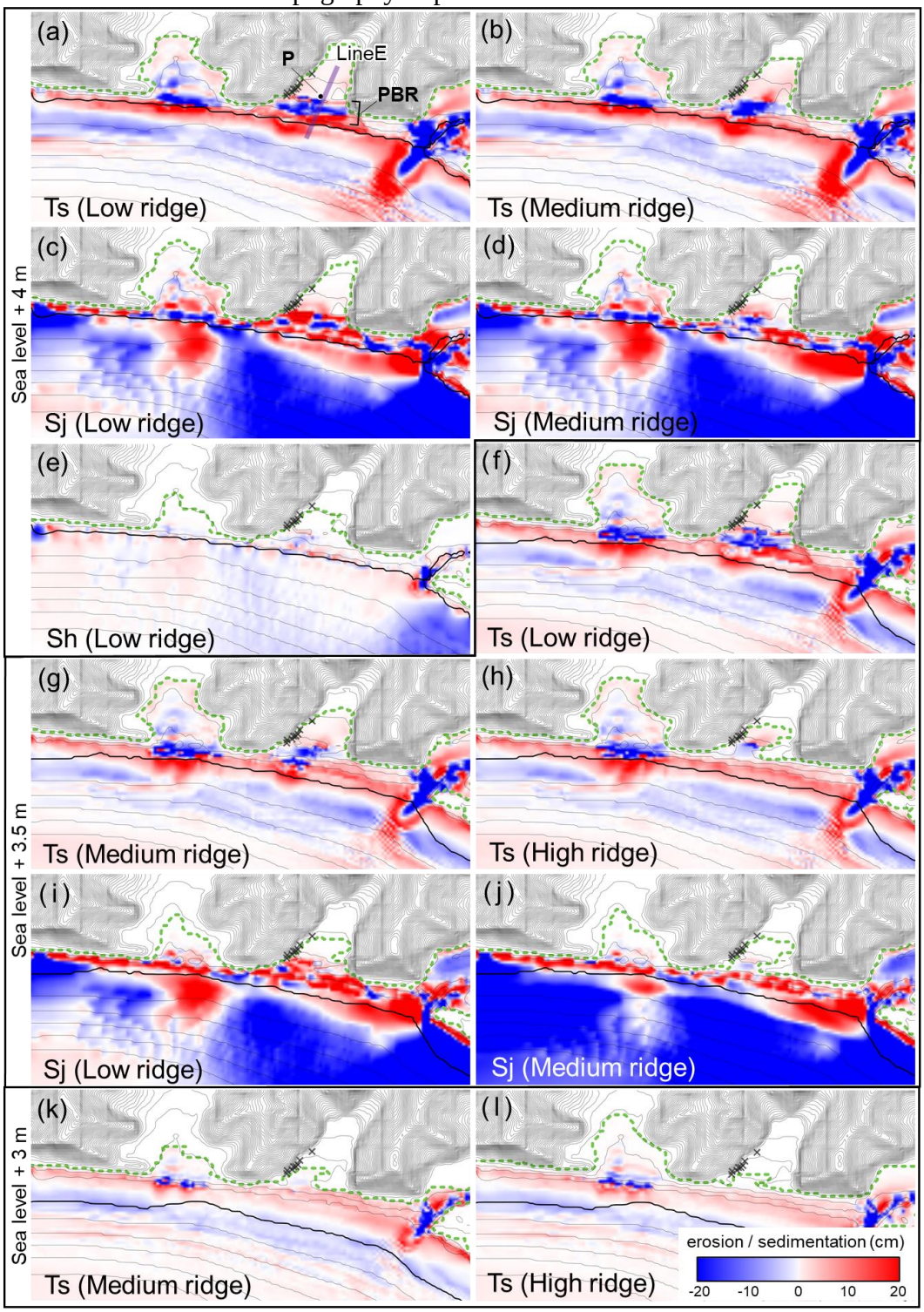

Figure 7. Cumulative sedimentation and erosion amount estimated using STM in the I area; the green dotted line indicates the maximum inundation area, and the black crosses indicate the distribution of EI-4.

4.3.1 4,000 BP (+ 4 m sea level)

The low and medium ridge scenarios were simulated at 4,000 BP because the PBR was not well developed (Nakanishi et al., 2022).

Tsunami model

The extent of the simulated tsunami inundation was 4–5 m asl (Figure 7ab). The estimated sediment distribution showed a sheet-like distribution of a few centimeters in the low ridge scenario (Figure 7a), whereas a localized, thick sand layer behind the PBR was confirmed in the medium ridge scenario (Figure 7b). Both ridge scenarios exhibited erosion at the top of and beyond the PBR, following outwash deposited in lobe-shape in shallow water.

The timeseries at point P (Figure 7a) of the medium ridge scenarios are shown in Figure 8. The overflow and sediment transport occurred in the first and the fifth to seventh waves. The first and sixth waves deposited 6- and 2-cm sand, respectively, but the layers were eroded by the return flow and the seventh wave, and the sand layer formed by the first wave remained. The transport mode was dominated by the suspension, and the grain-size composition was almost equal amounts of fine and coarse components.

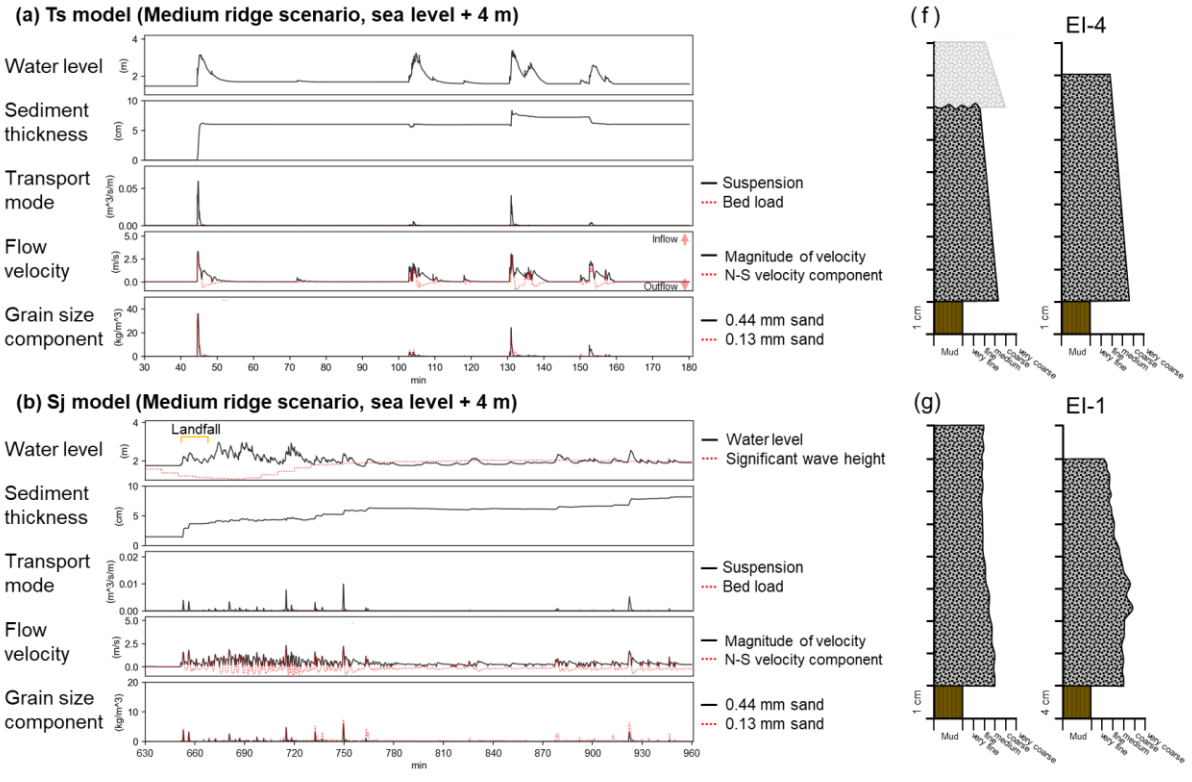

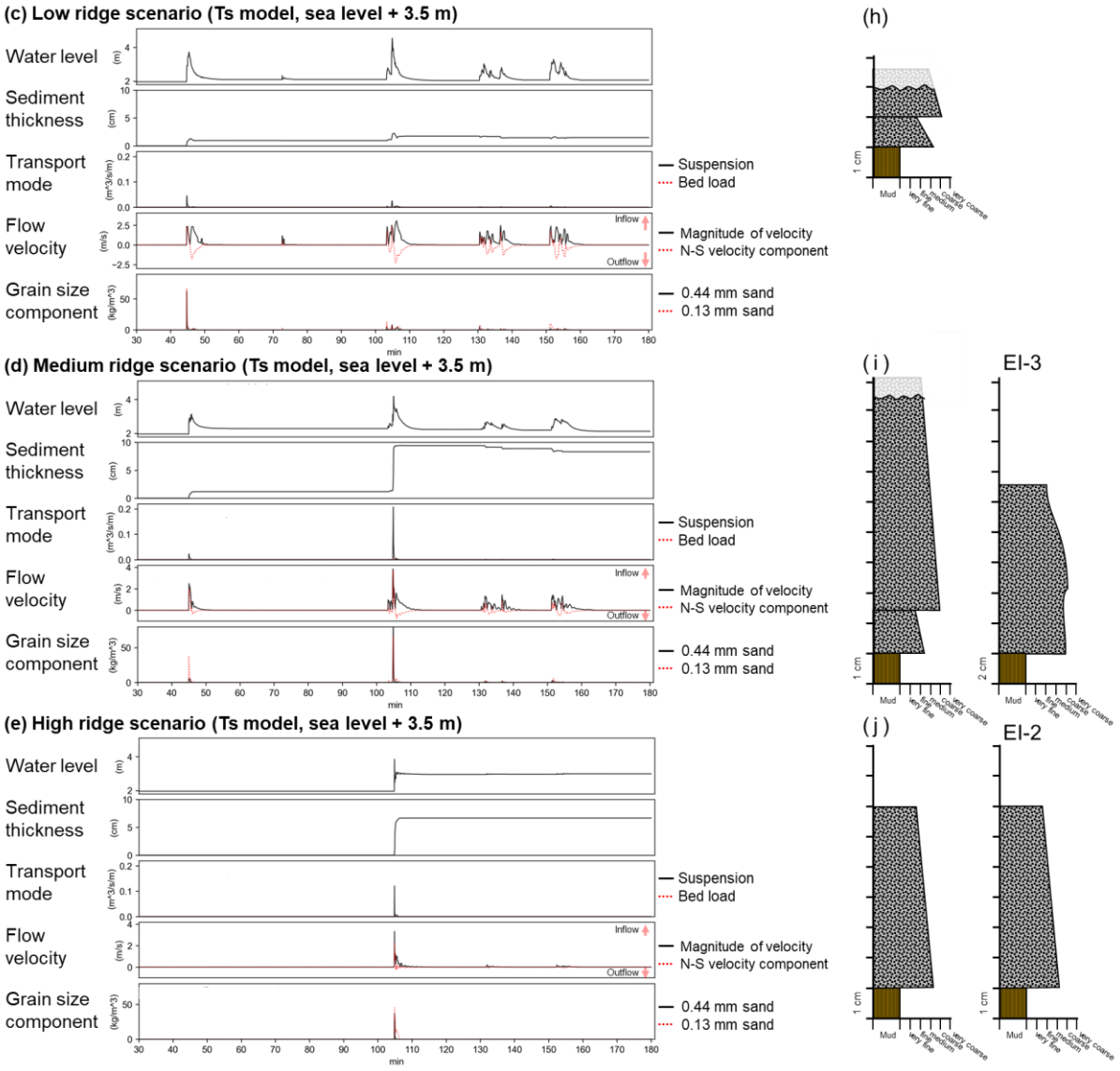

Figure 8. Timeseries of hydrodynamic and sediment transport and sedimentary structures estimated using STM at point P (Figure 7a). The Ts (a) and Sj (b) models in the medium ridge scenarios, and the low (c), medium (d), and high (e) ridge scenarios of the Ts model show the timeseries of water level, sediment thickness, transport flux in each transport mode, flow velocity, and transport flux of each grain-size composition. The sedimentary structures inferred from the Ts (f) and Sj (g) models in the medium ridge scenarios, and the low (h), medium (i), and high (j) ridge scenarios of the Ts model. Columnar diagrams of the sand layers observed at LA7 (Figure 1c) are shown for comparison.

Storm models

In the low ridge, the extent of the inundation by the Sh and Sj models was 3–5 m asl (Figure 7ce). In the medium ridge scenarios, the Sh model exhibited no inundation beyond the PBR, but the Sj models showed ~4 m asl of inundation (Figure 7d). The sediment distribution estimated using the Sh model was limited to around the PBR (Figure 7e). The Sj model showed a gradual inland thinning inland, and the lower ridge scenario formed a thicker sand layer slightly further inland.

The simulated sediments using the Sj model (medium ridge scenario) were repeatedly deposited and eroded for more than 300 min after landfall (Figure 8b), following an additional 2-cm thick sand layer deposited by storm waves. The dominant transport mode was suspension. Up to 720 min, the grain-size composition was almost equal amounts of fine and coarse components, but as the influence of the storm waves decreased, the fine component became dominant.

4.3.2 3,500 BP (+ 3.5 m sea level)

Tsunami model

All ridge scenarios showed inundation up to 3–4 m asl over the PBR (Figure 7f–h). The low ridge scenario formed a thin sheet-like layer in the medium and high ridge scenarios, showed a localized thick layer beyond the PBR, and showed gradually thinning inland. In the medium ridge scenario, the relatively lower part of the PBR was eroded, following sand deposited beyond the PBR or discharged into the sea (Figure 7g). In the high ridge scenario, the area beyond the PBR was eroded, and no sand was discharged to sea by the subsequent return flow (Figure 7h).

A timeseries of the hydrodynamic and sediment transport at point P beyond the PBR was compared for each ridge-height scenario (Figure 8c–e). In the low ridge scenario, sand layers were deposited in the first and fifth waves, but the final layer thickness was only ~2 cm (Figure 8c). A fast return flow with the same velocity as the inflow was observed. In the medium ridge scenario (Figure 8d), a 9-cm sand layer was deposited by the first and fifth waves, but 1.5-cm sand was then eroded by the sixth and seventh waves. The grain size of the sand layer was dominated by the fine component in the first wave, and the coarse component exceeded the fine component in the fifth wave. Most sand layers were transported by suspension, with limited bedload transport. In the high ridge scenario, the fifth wave created sediment transport by suspension, forming a 6-cm sand layer (Figure 8e). The grain-size composition showed a slightly higher proportion of the fine component than the coarse component.

Storm models

In the Sh models, no PBR overflow was observed, even in the low ridge scenario. The Sj models inundated over the PBR up to ~3 m asl in the low and medium ridge scenarios and the inundation area was the same in both scenarios (Figure 7ij). Meanwhile, no overflow occurred in the high ridge scenario. The low ridge scenario showed erosion and sedimentation of the entire PBR, whereas the medium ridge scenario showed inundation from a relatively lower part of the PBR and a small amount of sedimentation in the I area.

4.3.3 3,000 BP (+ 3 m sea level)

Because the depositional environment in this period was a closed freshwater swamp (Nakanishi et al., 2022), the medium and high ridge scenarios were employed. In the Ts model, overflow was observed in both ridge scenarios, but little deposition occurred over the PBR (Figure 7kl). In the storm model, no inundation occurred over the PBR in either scenario.

5 Discussion

5.1 Variation in Simulated Sediments According to Selected Parameters

5.1.1 Roughness coefficient

A roughness coefficient is related to a friction velocity, thereby affecting entrainment from a sediment source and a reduction in velocity. Many studies reported that the roughness coefficient of the source area and the inland area has a significant influence on the distribution of sediments (e.g., Li et al., 2014; Sugawara et al., 2014a). The tsunami simulations formed thick sediments in low roughness-coefficient scenarios, and their distribution tended slightly to extend inland (Figures 3 and 9). The roughness coefficient of the sand source area was a controlling factor for the layer thickness rather than the sediment distribution area because of its effect on the extent of erosion. The roughness coefficient on land, which is related to flow deceleration, is unaffected by a difference of ~0.01 $m^{-1/3}s$ (Figure 3). The results means that these uncertainties can be reduced by obtaining information on the depositional environment through light-element and diatom analyses. The storm simulations formed thicker sediments in the lower roughness-coefficient scenarios, whereas the distribution did not change significantly. Because of the potential for differences between tsunami and storm simulations, the roughness coefficient should be properly set based on geologic data.

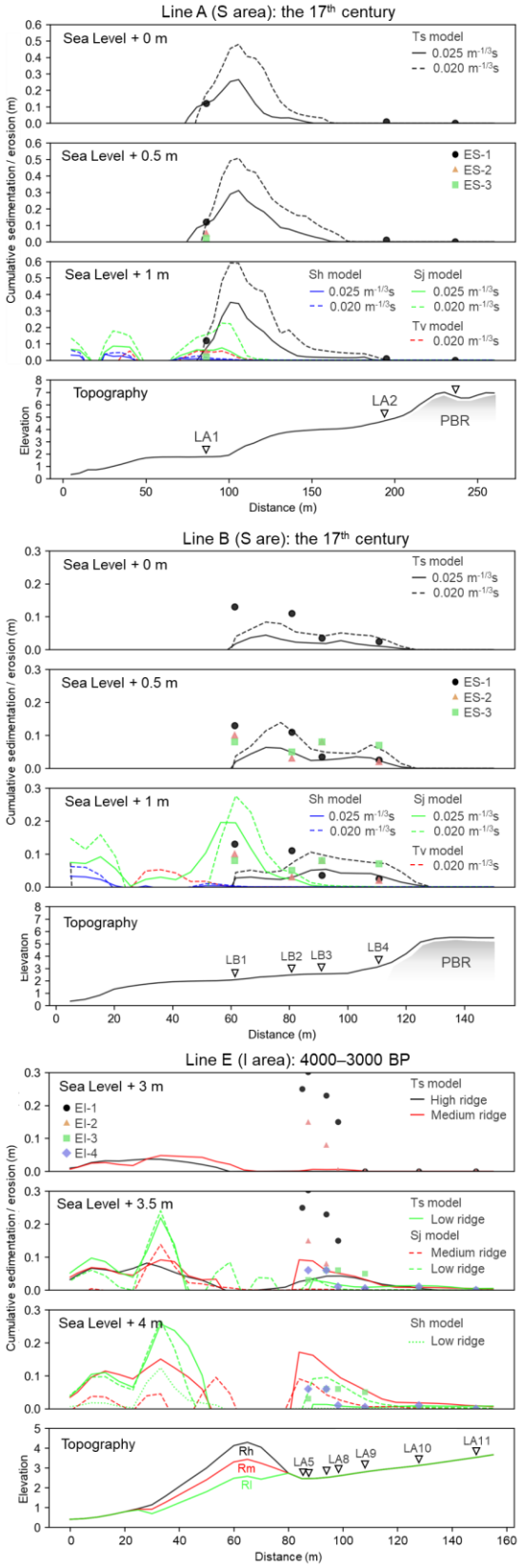

Figure 9. Thicknesses of the observed sand layers (indicated by markers) and estimated layer thicknesses using STM on the survey lines (Figure 1).

5.1.2 Initial source-sand area

It has been reported that when an initial source sand area is limited by a bottom sediment type, the calculated sediment distribution and thickness are also very restricted (Apotsos, 2011b; Li et al., 2014). The sensitivity tests indicated that if an unrealistically wide initial sand source is set up due to unclear bottom sediment quality in the prehistoric period, sand will be supplied from areas where the bottom sediment is essentially mud and the estimated sediment distribution will be overestimated (Figure 3). However, the unlimited initial source area scenarios displayed the sediment distribution that covered the observed sand layer on Line B, even in the medium sea-level scenario, because the sand was eroded slightly further inland than the setting initial source area, suggesting that a slight change in the source area causes significant variation in the estimated sediment distribution. Because the little geological data may have overlooked local sand sources, especially when the event layers are limited to the coastal area, a more comprehensive geological investigation is required.

5.1.3 Paleotopography and bathymetry

The importance of coastal topography in STM is emphasized by 2D modeling with different slopes (Watanabe et al., 2021; Gusman et al., 2012). The I and S areas have different coastal topography on the coastline, beach ridge height and the river mouth (Figure 1ef). The simulated tsunami entered the S area only at the river mouth, thus its location and width or length may affect the simulation results. The sediment thickness profiles are considerably affected by different topographies (Figure 9) as a thick layer in front of a steep slope (100 m from the coastline) on Line A and distributed in sheets on Line B. Meanwhile, the sedimentary structures are common to both Lines A and E (Figures 6 and 8). Sedimentary structures reflecting wave characteristics are not as sensitive to the topography as layer thickness distributions and may be useful proxies even when there is high uncertainty in the paleotopography. Storm deposits are more sensitive to topographic effects because the amounts of sand transported by the Sj model were larger and more inland in the I area than in the S area (Figures 5h and 7c). The simulated storm sediments showed that high waves and sediment transport occurred in a specific wind direction because the S area is located at the end of a path that leads through the intricate topography of the river mouth (Figure 5). This result can be explained by the narrow topography as a gate for waves in the S area, whereas the I area is directly connected to the beach across the PBR.

Bathymetries are uncertainties owing to the difficulty reconstructing more than paleotopography. The sensitivity tests showed that extreme gently sloping bathymetries underestimate onshore sediment distribution (Figure 3). When the sea transgressed, a simple interpolation between the highstand shoreline and the current bathymetry resulted in the reconstruction of these extremely gently sloping bathymetries. Such bathymetries are unrealistic when considering the dynamic equilibrium of the shoreline; therefore, the shallow-water bathymetry using the knowledge of coastal evolution must be reconstructed. Moreover, no significant effects were observed on extremely steep slopes. Therefore, the bathymetry uncertainty used in the STM for 4,000–3,000 BP should influence the results minutely.

5.1.4 Beach ridge height on coastal evolution process

The height of the beach ridge has a significant impact on not only overflow but also the amount of erosion and sedimentation caused by supercritical flows (Sugawara, 2019). The simulated results for the I area showed that the estimated sediment distribution changed significantly depending on the beach ridge height. In the low ridge scenarios, the estimated sediment thickness was thin because the sediments, once transported to the I area, were discharged directly to the sea by return flow (Supporting information S3). In the medium ridge scenarios, localized thick sedimentation occurred beyond the PBR because the beach ridge decreased the inflow velocity and the suspended sand was deposited beyond the PBR (Figures 7bg and 8ac). The return flows were also depressed by the ridge, preventing the sand from flowing out to the sea. In the high ridge scenarios, if the difference between sea-level and top of ridge was more than 3.5 m, the simulated tsunami could not overflow the PBR due to prevention by the high ridge (Supporting information S4). Higher sea-level scenarios showed thinner sediments, even if the ridge was well developed (Figure 7h). In this case, the overflow was trapped by the PBR, and sand transported by suspension settled in a near-hydrostatic state because the water level is constant after inundation (Figure 8e). Ridge development varies on the order of hundreds to thousands of years, which has important implications for reconstructing of tsunami deposits from earthquakes with an interval of several hundred years.

5.1.5 Relative sea level

The simulated results showed that the higher sea level, the more inland the inundation and sediment transport, but the effect on the sediment thickness and distribution was less than that of the beach ridge height. However, sea level changes were critical factors in STM because they are related to the development of a beach ridge.

5.2 Comparing Simulated Sediment of Tsunami and Storm

Differences were found in the areas where erosion and sedimentation occurred for tsunami and storm STM. The simulated tsunamis eroded in the areas of variable velocities, such as beach ridges and river mouth, and the transported sediments showed a sheet-like sand layer that extended inland (Figures 5 and 7). The simulated storms tended to erode heterogeneously along the coastline, depositing thick deposits at relative lows in the nearshore area. The difference between the sediment distribution and the inundation area was larger than that for the tsunami models. This difference between the distribution of tsunami and storm deposits was similar to that of STM in the Tohoku region (Watanabe et al., 2018). Tsunamis transport a larger amount of sediment inland than storms because of their high velocity on land, resulting in a wide sheet-like distribution of sediments. Meanwhile, storms show wide inundation of lowlands with gentle slopes, but the distribution of sediments is limited to near the shoreline, and longer inundation duration tends to produce thicker sediments. These characteristics were also observed in the complex topography as the S area and in closed topography with ridge topography as the I area.

The sedimentary structures of the sand layers were inferred from the timeseries of the hydrodynamic and sediment transport (Figure 6). The sedimentary structure of the Ts model was estimated to be a single normal grading because the transport mode was suspension and the final deposition was a single transport flow (Figures 6c and 8fhij). Moreover, the simulated storm sediments were estimated the repeated graded structures or massive structures because the flow velocity repeatedly increased and decreased at intervals of a few minutes. Overall, it shows a

normal or inverse grading structure reflecting changes in wind speed (Figures 2, 6d and 8g). The observed tsunami and storm deposits are distinguished by their sedimentary structures (e.g., Morton et al., 2007). Tsunamis form grading structure units depending on the number of inflows and outflows, whereas storms often form many overlapping laminasets that generally show either normal or inverse grading (Morton et al., 2007). These features are consistent with the sedimentary structures inferred from the timeseries variation in transport mode and grain size composition by STM. Sedimentary structures estimated using STM are a proxies to identify tsunami sediments even when it is difficult to distinguish based on sediment distributions.

5.3 Consistency Between the Observed and Simulated Sediments

5.3.1 7th–17th century event layers (S area)

The simulated and observed layer thicknesses were compared along Lines A and B to estimate the wave sources (Figure 9). For the Sj model, no sand was transported inland where sand layers were observed at LA2, LB3, and LB4. Therefore, we concluded that storm models were unrealistic for the formation of the event layers in the S area. The Tv model transported little sand inland. Only the + 1-m sea level (source roughness of 0.020 $m^{-1/3}s$) scenario of the Ts model showed the estimated sediments were distributed up to the observed sand layer at LA2. The estimated sedimentary structures were similar to ES-1 in that they show a single-normal grading structure (Figure 6c). Therefore, the Ts model is a realistic candidate for the 17th century event. The significant changes in the depositional environment, such as close to open brackish water, or floodplain to upland environments, have been reported after the deposition of ES-1 and ES-2 at LA1 (Nakanishi et al., 2022). The Ts model indicated that large scale erosion and sedimentation occurred over the land near the river mouth (Figure 5a–f), suggesting that the environment has been temporarily opened due to erosion or changed to an upland environment due to rapid deposition.

5.3.2 4,000–3,000 BP event layers (I area)

STM using the realistic largest typhoon (Sh) in Hokkaido was found to be inadequate enough to transport a sand layer into the I area (Figure 7e). The sediment distribution estimated by the Sj model covered the observed distribution in both low and medium ridge scenarios, with a tendency to thin inland (Figure 9). The scenarios where the sea level fell to + 3.5 m would not cover the observed sand layers. The unrealistic scale of the Sj model in Hokkaido suggested that a tsunami is a more plausible cause for the formation of EI-3 and EI-4. The sedimentary structures of the simulated storm sediments were unobserved in EI-2, EI-3, and EI-4 (Figure 8), but they were similar to those of EI-1, which was repeatedly graded and became finer overall (Nakanishi et al., 2022). However, considering the sea level during the deposition of EI-1 and the height of the PBR, it was unlikely that EI-1 was transported beyond the back-barrier, even by an overestimated typhoon.

As described by Nakanishi et al. (2020, 2022), the simulated results also showed that tsunami deposits were formed only during limited periods due to sea level changes and the development of beach ridges. The low ridge scenario results that only the thin and slight sand layers were formed (Figure 9) was consistent with the survey results that no clear event layer observed in the supratidal and high marsh environments before 4,000 BP (Nakanishi et al., 2022). The high ridge and low sea-level scenarios were recognized as most closely representing the topography after EI-1 deposition. The simulation results that no sand was transported to the I

area (Figure 7kl) was consistent with no event layer being observed in the I area after 3,000 BP (Nakanishi et al., 2022). The medium ridge scenario most closely represented the ridge height between the supratidal (~4,000 BP) and the fixed height of the PBR (~2,000 BP). Therefore, it was considered that these topographic conditions were closest to those during the deposition of EI-1 to EI-4. The medium ridge scenario of Ts model showed the sediment distribution with a gradual decrease inland from 10 cm (Figure 9). This was generally consistent with the observed thickness changes of EI-3 and EI-4. However, quantitative comparisons were difficult because the detail layer thickness was sensitive to many factor (e.g., microtopography or postdepositional effects). The estimated sedimentary structure also comprised multiple or single normal grading units, which was similar to the sedimentary structure of EI-3 and EI-4, respectively (Figure 8fi). Following this period, in the high ridge scenario, there is a pronounced normal grading structure with finer sand as EI-2 because a stagnant water condition continued due to the inhibition of the return flow by the PBR (Figure 8j). The tsunami that inundated the I area stressed not only the beach but also the area behind the PBR and cliffs, suggesting that erosion occurred on the beach to peatland (Supporting information S5). The diatom assemblage analysis suggested that the tsunami eroded the seaward ground surface and Paleogene cliffs because the event layers include brackish or Paleogene species (Nakanishi et al., 2022). The results of the STM scenarios as coastal evolution from high sea level and low ridge to low sea level and high ridge generally agree with the interpretation of the event stratigraphy, indicating that the setting parameters are reasonable. The STM of paleotsunami is useful not only for identifying the wave source but also for studying the formation potential of event layers.

5.4 Wave Source of Tsunami Deposits in the Shizunai Area

The event layer around the 17th century (ES-1) is probably the tsunami deposit because of its similarity in the sedimentary distribution and structures with the sediments calculated using the Ts model. Considering the low probability of the assumption that the sea level is + 1 m, which is a high tide in the 17th century (Figure 2), the Ts model (Nakanishi et al., 2021) is the minimum fault model reconstructing the tsunami deposits in the Shizunai area in the Kuril Trench. The volcanic tsunami model did not cover the observed sand layer distribution, and this source model did not account for the collapse process of a debris inflow. Delft-3D cannot account for the highly dispersive nature of volcanic tsunamis (Aptosos et al., 2011a). Therefore, it is necessary to develop a more accurate tsunami source model and a suitable tsunami propagation simulation for a STM in this area. The observed event layers from 4,000 to 3,000 BP (EI-1, EI-2, and EI-3) were reproduced by the 17th-century earthquake model using different paleotopographies. Earthquakes of comparable magnitude to the 17th-century earthquake in the Kuril Trench were found to be one of the wave source candidates to explain this tsunami deposit. EI-1, with a layer thickness of more than 30 cm, was not reproduced by the tsunami and storm models in all scenarios; however, the sedimentary structure was similar to those of the simulated storm deposits. To identify the wave source of EI-1, it will be necessary to survey the surrounding area to examine the regional extent of the event layer.

Although the 17th-century tsunami model is based on tsunami deposits in eastern Hokkaido (Nanayama et al., 2003; Satake et al., 2008; Sawai et al., 2009; Ioki & Tanioka, 2016; Nakanishi et al., 2021), it was found that the 17th century sand layers in the Shizunai area, far west of the Kuril Trench, can be reproduced by a realistic parametric model. However, this rupture zone may be more expansive because it simultaneously reconstructs the distribution of

tsunami deposits from western Hokkaido and the Kuril Islands (Ioki & Tanioka, 2017; Sawai, 2020). If the 17th century earthquake had a rupture zone extending further west that simultaneously reproduced the tsunami deposits in western Hokkaido (Takashimizu et al., 2007, 2017), the tsunami height in this area is even higher (e.g., Tetsuka et al., 2020), and the discrepancy between the observed and calculated sediments would be larger. Therefore, the magnitude of the present fault model on the southwest side of the Kuril Trench is generally appropriate. However, we cannot eliminate the possibility of Mw > 8 earthquakes in areas that have not been considered (e.g., off Hidaka or Shimokita Peninsula). On the other hand, sedimentary units of tsunami deposits, which are final traces of repeated deposition and erosion, have the potential to reconstruct wave information such as the number of overflows and the timing of the peak (Li et al., 2012). This STM results by far- to intermediate-field tsunamis model with predominant edge waves from the Kuril Trench were the peak wave of the last wave and thus renewed most of the previous sediments (Figures 6 and 8). Near-field tsunamis with a peak first wave may have formed multiple grading units, reflecting the decaying subsequent waves.

6 Conclusion

Through the STM of Kuril Trench earthquake-generated tsunamis, volcanic tsunamis, and storm surges/waves, we identified the origin of event layers in the Shizunai area located on the Hidaka coast of Hokkaido. The STM of prehistoric events demonstrated by constraining the numerical parameters using sensitivity tests based on detailed geological surveys. In sensitivity tests of several uncertainty parameters, the beach ridge height and the distribution of the initial sand-source considerably influenced the estimated sediment distribution and sedimentary structures. In particular, a high beach ridge prevents a tsunami overflow inland, whereas an excessively low height causes sand discharge by return flow; these results can reasonably explain the depositional period of the event layers on the coastal evolution processes. In Delft-3D, the initial source sediment thickness can be set for multiple grain sizes, enabling comparisons of the simulated results with sedimentary structures observed in geological surveys, even if the origin of event layers cannot be determined from the layer thickness or distribution. This study provided geological information that should be collected when applying STM to paleotsunamis, and showed that STM are an effective tool for identifying wave sources and tsunami deposits by taking this information into account even in prehistoric periods.

The tsunami event by the earthquake model in the Kuril Trench was sufficient to reproduce some sand layers observed over the past several thousand years in the Hidaka region, indicating that the western extension of the rupture zone is almost reasonable. STM through tsunami deposits in the same period in several regions can estimate the magnitudes of paleoearthquakes. As more tsunami deposits along the Pacific coast of Hokkaido are studied, the extent of the rupture zone in the Kuril Trench should become more clarified. In particular, STM in several areas along the Hidaka coast will be useful for estimating the minimum seismic magnitude at which tsunami deposits form and for constraining the detailed fault parameters in the Kuril Trench.

Acknowledgments

This research was supported by Grant-in-Aid from the JSPS to R. Nakanishi (20J21239).

Open Research

Data Availability Statement

This work relies on open-source code, namely Delft3D-Flow version 3.15 (Deltares, 2020) for sediment transport modeling (https://svn.oss.deltares.nl/repos/delft3d/tags/delft3d4/66766). This code requires registration to download. Tide level data for the past three years were obtained from the JODC Data On-line Service System (Japan Oceanographic Data Center, 2022, April 26: https://www.jodc.go.jp/jodcweb/JDOSS/index.html). Both sites include translation functionality.

References

Abe, T., Goto, K., & Sugawara, D. (2012). Relationship between the maximum extent of tsunami sand and the inundation limit of the 2011 Tohoku-oki tsunami on the Sendai Plain, Japan. *Sedimentary Geology*, *282*, 142–150. https://doi.org/10.1016/j.sedgeo.2012.05.004

Apotsos, A., Buckley, M., Gelfenbaum, G., Jaffe, B., & Vatvani, D. (2011a). Nearshore Tsunami Inundation Model Validation: Toward Sediment Transport Applications. *Pure and Applied Geophysics*, *168*(11), 2097–2119. https://doi.org/10.1007/s00024-011-0291-5

Apotsos, A., Gelfenbaum, G., Jaffe, B., Watt, S., Peck, B., Buckley, M., & Stevens, A. (2011b). Tsunami inundation and sediment transport in a sediment-limited embayment on American Samoa. *Earth-Science Reviews*, *107*(1–2), 1–11. https://doi.org/10.1016/j.earscirev.2010.11.001

Apotsos, A., Gelfenbaum, G., & Jaffe, B. (2011c). Process-based modeling of tsunami inundation and sediment transport. *Journal of Geophysical Research: Earth Surface*, *116*(F1). https://doi.org/10.1029/2010JF001797

Booij, N., Ris, R. C., & Holthuijsen, L. H. (1999). A third-generation wave model for coastal regions: 1. Model description and validation. *Journal of Geophysical Research: Oceans*, *104*(C4), 7649–7666. https://doi.org/10.1029/98JC02622

Bruun, P. (1962). Sea-Level Rise as a Cause of Shore Erosion. *American Society of Civil Engineers Journal of the Waterways and Harbours Division*, 88, 117–130.

Deltares. (2020). Delft3D-FLOW: Simulation of multi-dimensional hydrodynamic flows and transports phenomena, including sediments. User Manual, Version 3.15, Revision 66766 [Software]. Deltares. https://oss.deltares.nl/web/delft3d/get-started

Imai, K., Maeda T., Iinuma, T., Ebina, Y., Sugawara, D., Imamura, F., & Hirakawa, A. (2015). Paleo tsunami source estimation by using combination optimization algorithm: case study of the 1611 Keicho earthquake tsunami. *Tohoku Journal of Natural Disaster Science*, *51*, 139–144 (in Japanese).

Gusman, A. R., Tanioka, Y., & Takahashi, T. (2012). Numerical experiment and a case study of sediment transport simulation of the 2004 Indian Ocean tsunami in Lhok Nga, Banda Aceh, Indonesia. *Earth, Planets and Space*, *64*(10), 817–827. https://doi.org/10.5047/eps.2011.10.009

Gusman, A. R., Goto, T., Satake, K., Takahashi, T., & Ishibe, T. (2018). Sediment transport modeling of multiple grain sizes for the 2011 Tohoku tsunami on a steep coastal valley of Numanohama, northeast Japan. *Marine Geology*, *405*, 77–91. https://doi.org/10.1016/j.margeo.2018.08.003

Holland, Van. G., B. Verheyen, S. Jacobs, W. Vandenbruwaene, S. Temmerman, P. Meire, P. Peeters, and J. D. Schutter (2010), Simulation ofhydrodynamics and transport of fine sediments in vegetated polders with a controlled reduced tide: Pilot project Lippenbroek, in Pro-ceedings of the 8th International Symposium on Ecohydraulics 2010 (ISE 2010), 1775–1782.

Ioki, K., & Tanioka, Y. (2016). Re-estimated fault model of the 17th century great earthquake off Hokkaido using tsunami deposit data. *Earth and Planetary Science Letters*, *433*, 133–138. https://doi.org/10.1016/j.epsl.2015.10.009

Jaffe, B. E., Goto, K., Sugawara, D., Richmond, B. M., Fujino, S., & Nishimura, Y. (2012). Flow speed estimated by inverse modeling of sandy tsunami deposits: results from the 11 March 2011 tsunami on the coastal plain near the Sendai Airport, Honshu, Japan. *Sedimentary Geology*, *282*, 90–109. https://doi.org/10.1016/j.sedgeo.2012.09.002

816 Japan Coast Guard (1982). Japan Coast Guard Bathymetric Chart (No. 6374), Eastern Part of Tomakomai. Basic
817 map of the sea in coastal waters (1:50,000).
818 Japan Oceanographic Data Center (2022, April 26). Tide (Hour Tidal Height) Data [Dataset]. Japan Coast Guard.
819 https://www.jodc.go.jp/jodcweb/JDOSS/index.html
820 Kaiser, G., Scheele, L., Kortenhaus, A., Løvholt, F., Römer, H., & Leschka, S. (2011). The influence of land
821 cover roughness on the results of high resolution tsunami inundation modeling. *Natural Hazards and Earth System*
822 *Sciences*, *11*(9), 2521–2540. https://doi.org/10.5194/nhess-11-2521-2011
823 Koike, K. & Machida, H. (2001). Atlas of Quaternary Marine Terraces in the Japanese Islands: Tokyo, University
824 of Tokyo Press (in Japanese).
825 Kotani, N., Imamura, F., & Shuto, N., (1998). Tsunami run-up simulation and damage estimation by using GIS.
826 *Proceedings of Coastal Engineering, JSCE, 45*, 356–360 (in Japanese).
827 Lesser, G. R., Roelvink, J. A., van Kester, J. A. T. M., & Stelling, G. S. (2004). Development and validation of a
828 three-dimensional morphological model. *Coastal Engineering*, *51*(8), 883–915.
829 https://doi.org/10.1016/j.coastaleng.2004.07.014
830 Li, L., & Huang, Z. (2013). Modeling the change of beach profile under tsunami waves: a comparison of selected
831 sediment transport models. *Journal of Earthquake and Tsunami*, *07*(01), 1350001.
832 https://doi.org/10.1142/S1793431113500012
833 Li, L., Qiu, Q., & Huang, Z. (2012). Numerical modeling of the morphological change in Lhok Nga, west Banda
834 Aceh, during the 2004 Indian Ocean tsunami: understanding tsunami deposits using a forward modeling method.
835 *Natural Hazards*, 64(2), 1549–1574. https://doi.org/10.1007/s11069-012-0325-z
836 Li, L., Huang, Z., & Qiu, Q. (2014). Numerical simulation of erosion and deposition at the Thailand Khao Lak
837 coast during the 2004 Indian Ocean tsunami. *Natural Hazards*, 74(3), 2251–2277. https://doi.org/10.1007/s11069-
838 014-1301-6
839 Morton, R. A., Gelfenbaum, G., & Jaffe, B. E. (2007). Physical criteria for distinguishing sandy tsunami and
840 storm deposits using modern examples. *Sedimentary Geology*, 200(3–4), 184–207.
841 https://doi.org/10.1016/j.sedgeo.2007.01.003
842 Nakajo, S., Mori, N., Yasuda, T., & Mase, H. (2013). Development of global stochastic tropical cyclone model
843 based on temporal correlation of tropical cyclone parameters. *Journal of Japan Society of Civil Engineers Ser B2*
844 *(Coastal Engineering)*, *69*(1), 64–76 (in Japanese with English abstract). https://doi.org/10.2208/kaigan.69.64
845 Nakanishi, R., & Okamura, S. (2019). Tsunami deposits from the 1640 Hokkaido Komagatake eruption, north
846 Japan: constraints on inundation heights and numerical simulation of volcanic debris avalanche-derived tsunami.
847 *Journal of the Geological Society of Japan*, *125*, 835–851 (in Japanese, with English abstract).
848 https://doi.org/10.5575/geosoc.2019.0032
849 Nakanishi, R., Okamura, S., Yokoyama, Y., Miyairi, Y., Sagayama, T., & Ashi, J. (2020). Holocene tsunami,
850 storm, and relative sea level records obtained from the southern Hidaka coast, Hokkaido, Japan. *Quaternary Science*
851 *Reviews*, *250*, 106678. https://doi.org/10.1016/j.quascirev.2020.106678
852 Nakanishi, R., Ashi, J., Miyairi, Y., & Yokoyama, Y. (2021). Spatial extension of the mid to late Holocene
853 sedimentary record of tsunamis along the Southern Kuril Trench, Hokkaido Japan. *Earth and Space Science Open*
854 *Archive*. https://doi.org/10.1002/essoar.10508687.1
855 Nakanishi, R., Ashi, J., Miyairi, Y., & Yokoyama, Y. (2022). Holocene coastal evolution, past tsunamis, and
856 extreme wave event reconstructions using sediment cores obtained from the central coast of Hidaka, Hokkaido,
857 Japan. *Marine Geology*, 443, 106663. https://doi.org/10.1016/j.margeo.2021.106663
858 Nanayama, F., Satake, K., Furukawa, R., Shimokawa, K., Atwater, B. F., Shigeno, K., & Yamaki, S. (2003).
859 Unusually large earthquakes inferred from tsunami deposits along the Kuril trench. *Nature*, *424*(6949), 660–663.
860 https://doi.org/10.1038/nature01864
861 Nishimura, Y., & Miyaji, N. (1995). Tsunami deposits from the 1993 Southwest Hokkaido earthquake and the
862 1640 Hokkaido Komagatake eruption, northern Japan. Tsunamis: 1992–1994, Pageoph Topical Volumes,
863 Birkhäuser Basel, 719–733. https://doi.org/10.1007/978-3-0348-7279-9_19
864 Okada, Y. (1985). Surface deformation due to shear and tensile faults in a half-space. *Bulletin of the*
865 *Seismological Society of America*, *75*(4), 1135–1154. https://doi.org/10.1785/BSSA0750041135
866 Okuno, J., Nakada, M., Ishii, M., & Miura, H. (2014). Vertical tectonic crustal movements along the Japanese
867 coastlines inferred from late Quaternary and recent relative sea-level changes. *Quaternary Science Reviews*, *91*, 42–
868 61. https://doi.org/10.1016/j.quascirev.2014.03.010
869 Romano, F., Piatanesi, A., Lorito, S., & Hirata, K. (2010). Slip distribution of the 2003 Tokachi-oki Mw 8.1
870 earthquake from joint inversion of tsunami waveforms and geodetic data. *Journal of Geophysical Research: Solid*
871 *Earth*, *115*(B11). https://doi.org/10.1029/2009JB006665

Satake, K. (2015). Geological and historical evidence of irregular recurrent earthquakes in Japan. *Philosophical Transactions of the Royal Society A: Mathematical, Physical and Engineering Sciences*, *373*(2053), 20140375. https://doi.org/10.1098/rsta.2014.0375

Satake, K., Nanayama, F., & Yamaki, S. (2008). Fault models of unusual tsunami in the 17th century along the Kuril trench. *Earth, Planets and Space*, 60, 925–935. https://doi.org/10.1186/BF03352848

Satake, K., Fujii, Y., Harada, T., & Namegaya, Y. (2013). Time and Space Distribution of Coseismic Slip of the 2011 Tohoku Earthquake as Inferred from Tsunami Waveform Data. *Bulletin of the Seismological Society of America*, *103*(2B), 1473–1492. https://doi.org/10.1785/0120120122

Sawai, Y. (2020). Subduction zone paleoseismology along the Pacific coast of northeast Japan — progress and remaining problems. *Earth-Science Reviews*, *208*, 103261. https://doi.org/10.1016/j.earscirev.2020.103261

Sawai, Y., Kamataki, T., Shishikura, M., Nasu, H., Okamura, Y., Satake, K., et al. (2009). Aperiodic recurrence of geologically recorded tsunamis during the past 5500 years in eastern Hokkaido, Japan. *Journal of Geophysical Research: Solid Earth*, 114(B1). https://doi.org/10.1029/2007JB005503

Sella, G. F., Dixon, T. H., & Mao, A. (2002). REVEL: A model for Recent plate velocities from space geodesy. *Journal of Geophysical Research: Solid Earth*, *107*(B4), ETG 11-1-ETG 11-30. https://doi.org/10.1029/2000JB000033

Stelling, G. S., & Van Kester, J. A. Th. M. (1994). On the approximation of horizontal gradients in sigma co-ordinates for bathymetry with steep bottom slopes. *International Journal for Numerical Methods in Fluids*, *18*(10), 915–935. https://doi.org/10.1002/fld.1650181003

Sugawara, D. (2019). On tsunami sediment transport modeling and uncertainties. *Quaternary Research*, *58*(2), 187–194 (in Japanese with English abstract). https://doi.org/10.4116/jaqua.58.187

Sugawara, D., Goto, K., & Jaffe, B. E. (2014a). Numerical models of tsunami sediment transport — Current understanding and future directions. *Marine Geology*, *352*, 295–320. https://doi.org/10.1016/j.margeo.2014.02.007

Sugawara, D., Takahashi, T., & Imamura, F. (2014b). Sediment transport due to the 2011 Tohoku-oki tsunami at Sendai: Results from numerical modeling. *Marine Geology*, *358*, 18–37. https://doi.org/10.1016/j.margeo.2014.05.005

Sugawara, D., Yu, N. T., & Yen, J. Y. (2019). Estimating a Tsunami Source by Sediment Transport Modeling: A Primary Attempt on a Historical/1867 Normal-Faulting Tsunami in Northern Taiwan. *Journal of Geophysical Research: Earth Surface*, *124*(7), 1675–1700. https://doi.org/10.1029/2018JF004831

Takashimizu, Y., Sagayama, T., Nishina, K., Oka, T., Nakamura, & Y., Nishimura, Y. (2007). A 17th-century tsunami deposit discovered on the eastern Iburi coast, Hokkaido, northern Japan. Quaternary Research (Daiyonki-Kenkyu), 46, 119–130 (in Japanese, with English abstract).

Takashimizu, Y., Nishina, K., Kawakami, G., Sato, Y., Okamura, S., Nakanishi, R., Tamura, M., Hirose, W., Takahashi, R., & Ishimaru, S. (2017). Identification of a 17th-century tsunami deposit on the northern Hidaka coast, Hokkaido, northern Japan. Quaternary Research (Daiyonki-Kenkyu), 56, 1–9 (in Japanese, with English abstract).

Tanioka, Y., Nishimura, Y., Hirakawa, K., Imamura, F., Abe, I., Abe, Y., et al. (2004). Tsunami run-up heights of the 2003 Tokachi-oki earthquake. *Earth, Planets and Space*, *56*(3), 359–365. https://doi.org/10.1186/BF03353065

Tetsuka, H., Goto, K., Ebina, Y., Sugawara, D., & Ishizawa, T. (2020). Historical and geological evidence for the 17th-century tsunami(s) along Kuril and Japan trenches: Implications for the origin of the AD 1611 Keicho earthquake and tsunami, and for the probable future risk potential. Geological Society, London, Special Publications, 501. https://doi.org/10.1144/SP501-2019-60

van Ormondt, M., Nederhoff, K., & van Dongeren, A. (2020). Delft Dashboard: a quick set-up tool for hydrodynamic models. *Journal of Hydroinformatics*, *22*(3), 510–527. https://doi.org/10.2166/hydro.2020.092

van Rijn, L.C. (1993). Principles of Sediment Transport in Rivers, Estuaries and Coastal Seas. Aqua Publications, Amsterdam.

Watanabe, M., Bricker, J. D., Goto, K., & Imamura, F. (2017). Factors responsible for the limited inland extent of sand deposits on Leyte Island during 2013 Typhoon Haiyan. *Journal of Geophysical Research: Oceans*, *122*(4), 2795–2812. https://doi.org/10.1002/2016JC012023

Watanabe, M., Goto, K., Bricker, J. D., & Imamura, F. (2018). Are inundation limit and maximum extent of sand useful for differentiating tsunamis and storms? An example from sediment transport simulations on the Sendai Plain, Japan. *Sedimentary Geology*, *364*, 204–216. https://doi.org/10.1016/j.sedgeo.2017.12.026

Watanabe, M., Goto, K., Roeber, V., & Imamura, F. (2021). Identification of Coastal Sand Deposits From Tsunamis and Storm Waves Based on Numerical Computations. *Journal of Geophysical Research: Earth Surface*, *126*(7), e2021JF006092. https://doi.org/10.1029/2021JF006092

Yokoyama, Y., Okuno, J., Miyairi, Y., Obrochta, S., Demboya, N., Makino, Y., & Kawahata, H. (2012). Holocene sea-level change and Antarctic melting history derived from geological observations and geophysical

928 modeling along the Shimokita Peninsula, northern Japan. *Geophysical Research Letters, 39*(13), L13502.
929 https://doi.org/10.1029/2012GL051983